Czech Technical University in Prague
Faculty of Nuclear Sciences and Physical Engineering

Department of Physics
Study programme: Nuclear and Particle Physics

Impact of Propagation of Cosmic Rays on their Properties Measured at the Highest Energies

DIPLOMA THESIS

Author:	Bc. Robert Hrubý
Supervisor:	Ing. Jakub Vícha, Ph.D.
Consultant	Ing. Alena Bakalová
Academic year:	2022/2023

České vysoké učení technické v Praze
Fakulta jaderná a fyzikálně inženýrská

Katedra fyziky
Studijní program: Jaderná a částicová fyzika

Vliv šíření kosmického záření na jeho vlastnosti pozorované na nejvyšších energiích

DIPLOMOVÁ PRÁCE

Vypracoval: Bc. Robert Hrubý
Vedoucí práce: Ing. Jakub Vícha, Ph.D.
Konzultant: Ing. Alena Bakalová
Rok: 2022/2023

ČESKÉ VYSOKÉ UČENÍ TECHNICKÉ V PRAZE
FAKULTA JADERNÁ A FYZIKÁLNĚ INŽENÝRSKÁ
PRAHA 1 - STARÉ MĚSTO, BŘEHOVÁ 7 - PSČ 115 19

Katedra: fyziky   *Akademický rok:*   2021/2022

ZADÁNÍ DIPLOMOVÉ PRÁCE

Student: Bc. Robert Hrubý

Studijní program: Jaderná a částicová fyzika

Název práce: Vliv šíření kosmického záření na jeho vlastnosti pozorované na
(česky)   nejvyšších energiích

Název práce: Impact of Propagation of Cosmic Rays on their Properties Measured at
(anglicky)   the Highest Energies

Pokyny pro vypracování:

1) Simulace propagace kosmického záření pro různé částice a vlastnosti jejich zdrojů
pomocí programu CRPropa 3.

2) Studium měřených vlastností kosmického záření ultra-vysokých energií.

3) Hledání vlastností zdrojů kosmického záření, které jsou v souladu s měřeními
Observatoře Pierra Augera ohledně anizotropie, složení a energetického spektra.

Doporučená literatura:

[1] A. Aab, et al.: Measurement of the cosmic ray energy spectrum above 2.5 x 10^18 eV using the Pierre Auger Observatory, Phys. Rev. D 102 (2020) 062005

[2] A. Aab, et al.: Indication of anisotropy in arrival directions of ultra-high-energy cosmic rays through comparison to the flux pattern of extragalactic gamma-ray sources, Astrophys. J. Lett. 853 (2018) L29

[3] A. Aab, et al.: Depths of maximum of air-shower profiles at the Pierre Auger Observatory: Composition implications, Phys. Rev. D 90 (2014) 122006

[4] Ch. Ding, et al.: The imprint of large scale structure on the ultra-high-energy cosmic ray sky, Astrophys. J. Lett. 913 (2021) L13

[5] R. A. Batista, et al., CRPropa 3 - a public astrophysical simulation framework for propagating extraterrestrial ultra-high energy particles, JCAP 05 (2016) 038.

Jméno a pracoviště vedoucího diplomové práce:

Ing. Jakub Vícha, Ph.D.
Fyzikální ústav AV ČR, v. v. i.

Jméno a pracoviště konzultanta diplomové práce:
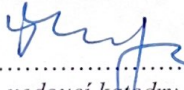Ing. Alena Bakalová
Fyzikální ústav AV ČR, v. v. i.

Datum zadání diplomové práce: 20.10.2021

Termín odevzdání diplomové práce: 02.05.2022

Doba platnosti zadání je dva roky od data zadání.

....
garant studijního programu

....
vedoucí katedry   *děkan*

V Praze dne   20.10.2021

P R O H L Á Š E N Í

Já, níže podepsaný

Jméno a příjmení studenta:	Robert Hrubý
Osobní číslo:	503096
Název studijního programu (oboru):	Jaderná a částicová fyzika

prohlašuji, že jsem diplomovou práci s názvem:

Vliv šíření kosmického záření na jeho vlastnosti pozorované na nejvyšších energiích

vypracoval samostatně a uvedl veškeré použité informační zdroje v souladu s Metodickým pokynem o dodržování etických principů při přípravě vysokoškolských závěrečných prací.

V Praze dne 02/05/23

....

podpis

Název práce:

Vliv šíření kosmického záření na jeho vlastnosti pozorované na nejvyšších energiích

Autor:	Bc. Robert Hrubý
Studijní program:	Jaderná a částicová fyzika
Druh práce:	Diplomová práce
Vedoucí práce:	Ing. Jakub Vícha, Ph.D.
	Oddělení astročásticové fyziky, Fyzikální ústav Akademie věd České republiky, v. v. i.
Konzultant:	Ing. Alena Bakalová
	Oddělení astročásticové fyziky, Fyzikální ústav Akademie věd České republiky, v. v. i.

Abstrakt: Studie zkoumala chování extragalaktického kosmického záření v energiích nad 40 EeV pomocí simulací v programu CRPropa 3. Při analýze byly zkoumány dva různé případy umožňující nalézt anizotropní signál: výběr nad a pod galaktickou rovinou a výběr vzhledem k pozorovanému dipólu ve směrech příletů kosmického záření. V případě výběru nad a pod galaktickou rovinou nebyl pozorován žádný významný hmotnostní rozdíl. Při rozdělení podle pozorovaného dipólu se ukazuje vyšší citlivost v hmotnostním rozdílu, nicméně rozdíly nedosahují hodnot pozorovaných Observatoří Pierra Augera. Dále byl testován vliv změny pozice extragalaktického dipólu kde se ukazalo ze ma vliv na anizotropii v hmotnostním rozdílu.

Title:

Impact of Propagation of Cosmic Rays on their Properties Measured at the Highest Energies

Author:	Bc. Robert Hrubý

Abstract: The study investigated the behaviour of extragalactic cosmic rays at energies above 40 EeV using simulations in CRPropa 3. The analysis examined two different cases allowing to find an anisotropic signal: selection above and below the galactic plane and selection relative to the observed dipole in the directions of cosmic ray arrivals. In the case of selection above and below the galactic plane, no significant mass difference was observed. However, selection according to the dipole shows a higher sensitivity in the mass difference. However, the difference does not reach the values observed by the Pierre Auger Observatory. Furthermore, the effect of changing the extragalactic dipole position was investigated and found to have an effect on the anisotropy in the mass difference.

List of Figures

Contents

Introduction

It has been a long time since the discovery of cosmic rays and even the recent ultra-high-energy cosmic rays (UHECR) are not so recent anymore, and yet there is still much to learn about them (13).

UHECR undergoes a hardening in the energy spectrum called the ankle (14). Above this energy, the flux has long been the hypothesis that it is primarily of extragalactic origin (15) which was also supported by the recent discovery of a dipole anisotropy in the arrival directions of UHECR with energies just above the ankle (11). Another indication of the extragalactic origin of UHECRs is the flux suppression at around 40 EeV where propagation should become less diffusive (11).

The mass composition at energies above 40 EeV is best described as a mixture of light, intermediate, and high-mass nuclei, such as protons, helium, nitrogen, and iron nuclei (16). Such a mixed composition shows that particles from their sources are modified during their propagation through the universe. Examples of properties that are modified are the arrival direction of the particles, the chemical composition of the particles, the energy of the particles. This can be caused by many factors, such as deflections in the extragalactic and galactic magnetic fields or more severe energy loss effects that depend primarily on the mass and charge (17). For that reason, it is important, if not vital, to study simultaneously the effect of propagation of cosmic rays from their sources to Earth together with measurements of UHECR on Earth by large-area observatories.

In this diploma thesis, we use an open-source simulation framework for the propagation of cosmic rays called CRPropa 3 (10). This in combination with real Monte Carlo simulations of the detector response at the Pierre Auger Observatory is used to investigate changes in mass composition anisotropy in the arrival directions of UHECR. $X_{\max}$ (depth of the shower maximum) is sensitive to mass and, therefore, allows us to analyse this behaviour. In addition to simulations, $X_{\max}$ can be well measured by modern observatories, which allows for a comparison between the observed and simulated mass anisotropy, which was recently observed by the Pierre Auger Observatory (9).

The first part of this diploma thesis will introduce a brief historical introduction together with some basic properties of cosmic rays. Then we proceed in Chapter 2 with the propagation of UHECR in the universe, their energy losses, and their interactions with background radiation. We also describe the model of the galactic magnetic field that is used and how it affects UHECR. In Chapter 3, the Pierre Auger Observatory is briefly described together with the different observation tech-

niques used. Chapter 4 is dedicated to the motivations and a closer look at the results observed at Pierre Auger, from which the idea for this thesis came. Chapter 5 includes some characteristics of simulation frameworks dedicated to the propagation of cosmic rays in the universe, together with other tailored parameters to achieve real conditions. Last but not least, the results for each of the analyses done and its findings are closely discussed, which is then followed by a conclusion.

Chapter 1

Ultra-High Energy Cosmic Rays

The discovery of cosmic rays serves as a prime example of how seemingly random noise can in fact contain valuable information.

Since the early 1900s, cosmic rays have been a subject of intrigue and speculation. Victor Franz Hess was one of the first physicists to conduct a series of experiments from 1911 to 1913 to reveal the truth about ionisation that was always present. These experiments involved measuring ionisation levels at different altitudes using a hot air balloon together with an electroscope to record data. In contrast to the prevalent hypothesis of the time, Hess's measurements revealed that ionisation levels increased with elevation, indicating that the radiation was not of terrestrial origin but rather coming from outer space. This pivotal discovery marked the dawn of a new era of exploration of the nature and sources of cosmic rays (13).

Another physicist, Pierre Victor Auger, together with Rossi, Boethe, Schmeiser, and Kolhorster, made a critical discovery by identifying extensive air showers of secondary particles from cosmic rays. This discovery played a fundamental role in the establishment of the Auger Observatory, as this is the signal on which the observatory is focused (2) as outlined in Section 3. It is established that cosmic rays are charged particles, with protons representing the majority of cosmic rays (approximately 86%), followed by helium nuclei (approximately 11%), and nuclei of heavier elements up to iron, with a mixed composition (18).

There also exist a subset of cosmic rays, which then represent highly energetic particles whose origin is believed to lie outside our galaxy. These are known for their high energies ranging from 10^{18} eV to 10^{20} eV or higher and are called ultra-high energy cosmic rays (UHECRs). Today, the origin of UHECR remains one of the primary enigmas in astroparticle physics. Although it is believed that they come from extragalactic sources, the particular sources and mechanisms of their acceleration are still not fully understood.

Investigating UHECRs poses several challenges due to their rarity. One of such challenges is that they are extremely rare, with only a few arriving to Earth per square kilometre per year. To study these particles, mainly ground-based observations are used; such as the Pierre Auger Observatory explained in Section 3.

Despite the amount of time since the discovery of UHECRs, a number of critical questions still remain unanswered, such as the nature of the primary cosmic rays, their most powerful energies, their potential sources and acceleration, the cut-off in their energy spectrum at the highest energies, which can be caused either by interactions with cosmic microwave background or by reaching the maximal accelerations, among others. Various theories about origin of UHECR have been proposed, which could include topics such as active galactic nuclei, gamma-ray bursts, among others.

In this chapter, we discuss the properties of cosmic rays, with a particular focus on UHECRs. The topics covered will include the energy spectrum and mass composition, as well as the relation to X_{max}.

1.1   Energy spectrum

The energy spectrum of cosmic rays has a wide range. This spectrum of cosmic rays is typically described as a power law, which means that the number of cosmic rays with energy E decreases as $\frac{dN}{dE} \approx E^{\gamma}$, where γ is a constant called the spectral index. This power-law behaviour is observed across many orders of magnitude in energy, from as low as 10^9 eV. to as high as 10^{20} eV.

Hence, the energy spectrum can be approximated with a spectral index of $\gamma \simeq -2.7$ below an energy of $E \approx 4 \cdot 10^{15}$ eV. However, the spectrum undergoes significant changes in behaviour at various energies. A steepening of the spectrum known as the "knee" occurs at an energy of $E \approx 10^{15.6}$ eV, where the spectral index changes to $\gamma \simeq -3.1$. Another steepening, called the "second knee," is observed around an energy of $\approx 10^{17}$ eV (19). The spectrum hardens at $E \approx 5 \cdot 10^{18}$ eV, known as the "ankle," with the spectral index changing to $\gamma \approx -2.5$. This is followed by a recently identified feature called the "instep." The spectrum ultimately reaches a cutoff at the highest energies of $\approx 4 \cdot 10^{19}$ eV (20) (6) see Figure: 1.1. These variations reflect on the mechanisms underlying the acceleration and generation of cosmic-ray particles for a given energy where factors such as particle rigidity[1] play an important role.

From the knee up to the ankle region, we see that the contribution of light elements to the spectrum is largely dominant, after which we see the heavier elements gradually take over, this is largely due to the fact that as Peters suggested, there is maximal energy to which protons can be accelerated this also applies so that different particles should be accelerated to different maximal energies depending on their rigidity. This causes protons to be cutoff first, follows by the other particles due to the apparent lack of sources in the Galaxy, which is capable of accelerating therefore they are wash out from the galaxy (21). This statement holds true up to the ankle at which the lighter particles from extragalactic sources starts to introduce themselves back see Figure: 1.3.

---

[1]Is a measure of a charged particle's resistance to bending due to magnetic fields defined as R = pc/q, where p is particle momentum, c speed of light, q is charge. Higher-rigidity particles are less affected by magnetic fields and its direction is less effected where as lower-rigidity particles direction is more effected by the field.

The cutoff at the end of the energy spectrum was predicted by Greisen (22), Zatsepin, and Kuzmin (23). They established a theoretical upper limit for the energy of protons emanating from distant sources, which corresponds to the very end of the energy spectrum. This maximum energy of the extragalactic proton results from photopion production in interactions with cosmic microwave background (CMB)[2]. Hence, the point where the spectrum falls is known as a GZK cutoff whose energy value corresponds to about $E \approx 10^{19.7}$ eV (for protons). This can be observed in the measurements done by the Pierre Auger Observatory and the Telescope Array, who managed to demonstrate this steep falling of the energy spectrum above $\approx 10^{19.7}$ eV (1).
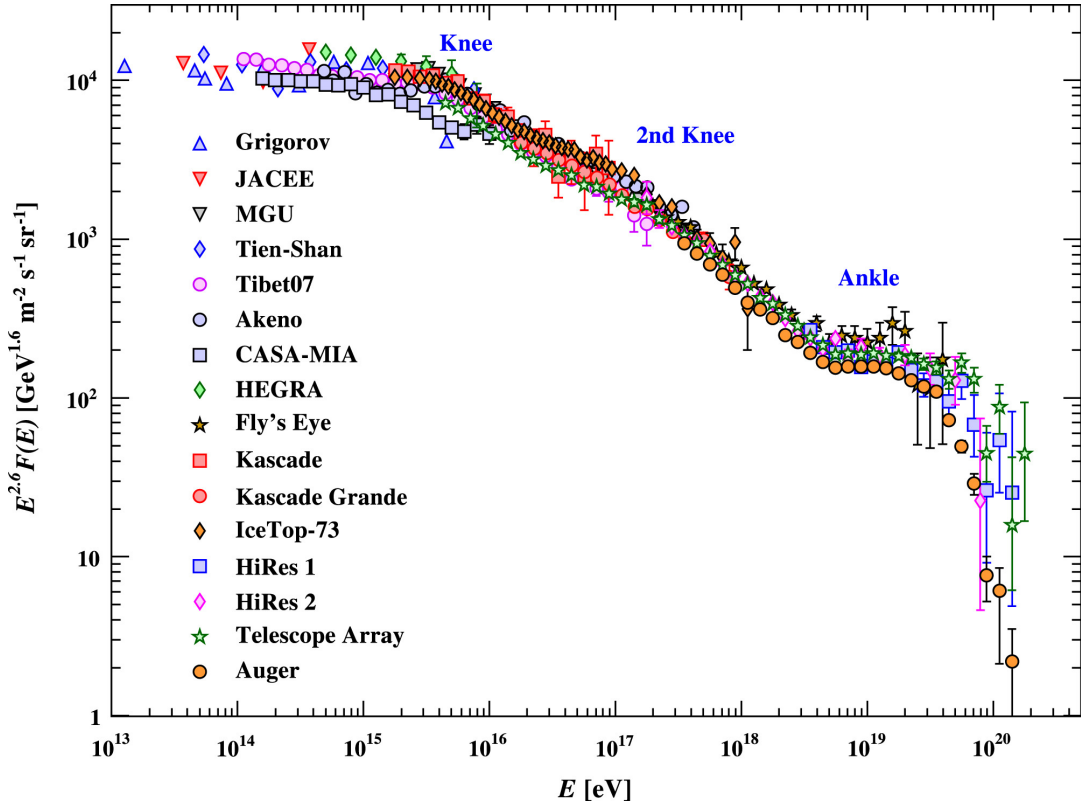
Figure 1.1: All-particle energy spectrum of cosmic rays. Note that the flux is scaled by $E^{2.6}$. Figure taken from (1).

---

[2]This radiation is a remnant from an early stage of the Universe, called the recombination, when the Universe became transparent to photons.

1.2 Mass Composition

The mass composition of cosmic rays varies with energy due to various factors, including the sources and its position, the magnetic field of the galaxy, and the effects of magnetic confinement. These factors can result in the dominance of certain nuclei over others at specific energies, which is important for understanding the physics behind the origin and propagation of cosmic rays. However, it is difficult to directly measure the mass composition of cosmic rays, as we can only detect the secondary particles produced in cosmic-ray showers from which the mass and energy of the primary particles can be deduced by closely analysing the properties of the longitudinal development of the shower cascade.

The development of the corresponding electromagnetic and hadronic cascade (24) also characterised more accurately as slant depth X, its obtained by integrating the air density along the direction of arrival of the air shower through the curved atmosphere, as in

$$X(z) = \int_z^\infty \rho(\vec{r}(z'))dz', \tag{1.1}$$

"where $\rho(r(z))$ is the density of air at a point with longitudinal coordinate z along the shower axis" (25). The specific depth at which the energy deposit reaches its maximum is called the depth of shower maximum, $X_{\max}$. This is important because it is proportional to the logarithm of the mass "A" where A refers to the nuclear mass of the primary particle; however, it is important to realise that due to the fluctuation of hadronic interaction in the cascade the primary mass cannot be measured on event-by-event basis. The only way this can be approached is statistically as a distribution. This, however, introduces numerous uncertainties, a detailed explanation can be found in (25). However for the purposes of this diploma thesis, it suffices to mention that the final uncertainty of $X_{\max}$ smearing is 20 g/cm^2 (25).

$X_{\max}$ can provide important information about the mass and energy of the primary UHECR (25), Its reconstruction is typically achieved by analysing the signals acquired from fluorescence detectors in conjunction with surface detectors which both are type of detectors used at Pierre Auger Observatory, more in dept discussion can be found in Section 3.

In general, we know that heavier primary particles will produce shallower showers meaning it will have lower $X_{\max}$ value and also narrower $\sigma(X_{\max})$ than lighter particles, which on the contrary will produce deeper $X_{\max}$ values and also wider $\sigma(X_{\max})$. Figure 1.2 gives us a visual representation of how each primary element (p, He, N, Fe) is related to a specific $X_{\max}$ distribution.
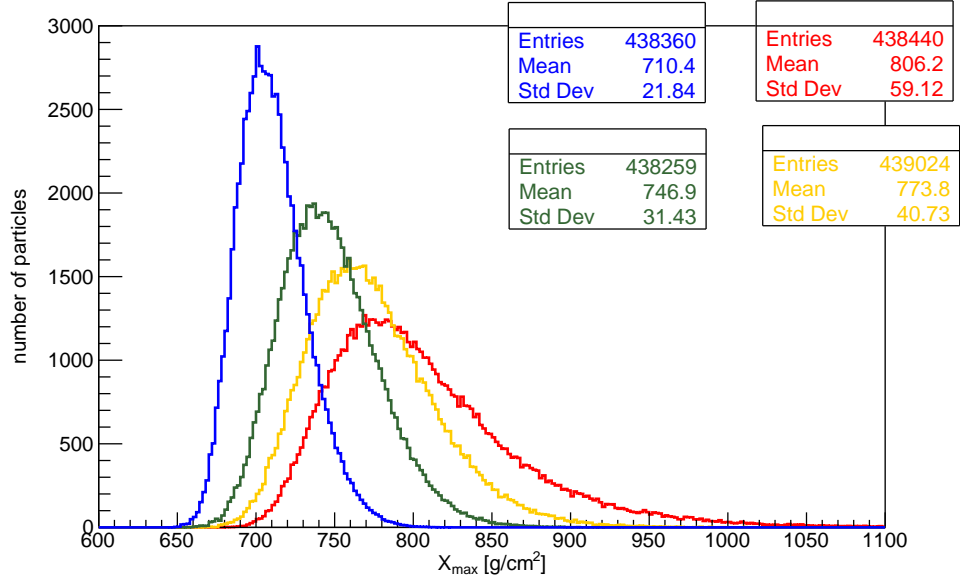
Figure 1.2: Shows a distribution of shower maxima for different primary particles at energy $10^{18.8}eV$. Red (Proton), orange (Helium), green (Nitrogen), and blue (Iron).
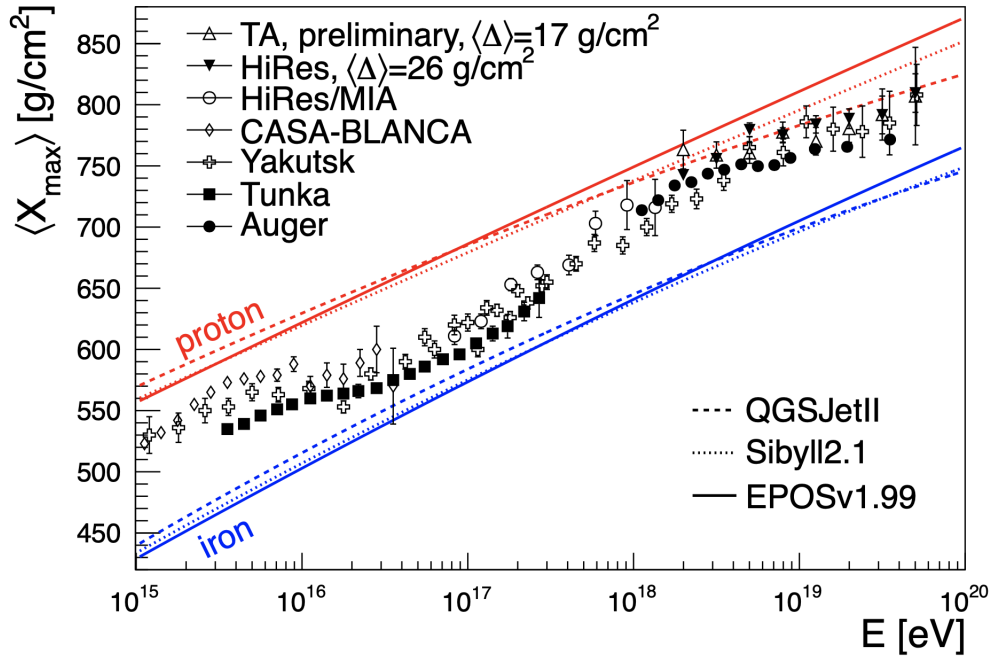
Figure 1.3: Measurements of the mean $X_{\max}$ with respect to energy from multiple experiments compared to QGSJet II, Sibyl II and EPOSv1.99 hadronic simulations (2).

Chapter 2

Propagation of Ultra-High Energy Cosmic Rays

The propagation of UHECRs in the universe is a complex and dynamic process that involves a range of physical phenomena. On their voyage UHECRs interact with the cosmic microwave background CMB which has a very small energy around 10^{-3} eV (26). In addition to that, UHECRs can also interact with optical and infrared backgrounds as well as radio waves. These interactions can cause energy losses and changes in their chemical composition. Another important factor in the propagation is the magnetic fields, which exist in the galactic and extragalactic medium. They can deflect the trajectories of the UHECRs, leading to a diffusion-like behaviour, which means that the arrival directions of the detected particles are not necessarily pointing to their origin.

Understanding these collective effects of the magnetic fields and background interactions and how they affect the UHECR propagation is essential for interpreting their observations.

In this section, we will briefly discuss some energetic losses that are relevant to the propagation of UHECRs, but we note that the focus of this diploma thesis is on their propagation within the Galaxy, where these losses can be neglected due to their relatively short distances (27). Furthermore, we will provide an overview of galactic magnetic fields (GMF) and extragalactic magnetic fields (EGMFs), with a greater emphasis on the galactic field, given the focus of this diploma thesis on interstellar propagation (28).

2.1 Energy Losses

2.1.1 *Photo-pion production*

One of the most significant energy losses is through the production of pions when the UHECR interact with the ambient photon background also called CMB or other photon backgrounds, such as the cosmic infrared background or the cosmic optical background. For head-on collision of nucleon with photon can be described as

$$N + \gamma \rightarrow N' + \pi, \tag{2.1}$$

with threshold

$$E_{thres}^{N,\pi} = \frac{m_\pi(m_N + \frac{1}{2}m_\pi)}{2\epsilon} \approx 6.8 \cdot 10^{19}\left(\frac{\epsilon}{10^{-3}eV}\right)^{-1} \text{eV}. \tag{2.2}$$

Where the m_π and m_N are the masses of the pion and nucleon, respectively, and ϵ is the average energy of background photons (28).

Due to the extreme inelasticity of the process and the density of CMB photons, it was understood in the 1960s that the cosmos is opaque for ultra-high energy particles, resulting in GZK flux suppression. An example of such production is given by

$$p + \gamma \rightarrow \Delta^+ \Longrightarrow \begin{cases} n + \pi^+ & \text{with branching ratio } 1/3 \\ \\ p + \pi^0 & \text{with branching ratio } 2/3 \end{cases} \tag{2.3}$$

Where in fact, they are the main channel for the production of ultra-high-energy secondary photons and neutrinos by hadronic cosmic rays (28).

2.1.2 *Pair production*

Another important process that contributes to energy losses is when a UHECR interacts with a photon from the CMB or other photon backgrounds, resulting in the creation of an electron-positron pair.

The energy threshold for this reaction is

$$E_{thres}^{\pm} = \frac{m_e(m_X + m_e)}{\epsilon} \approx 4.8 \cdot 10^{17} A(\frac{\epsilon}{10^{-3}eV})^{-1}\text{eV} \tag{2.4}$$

where m_e and m_x are the masses of the electron/positron and of nucleus X respectively, and ϵ represent the energy of the background photon (28). Due to its low threshold, this process is typically treated as a continuous energy loss process (28).

2.1.3 *Photodisintegration*

Photodisintegration of nuclei is another common process in which an atomic nucleus absorbs a photon, causing it to enter an excited state before disintegrating into two or more particles. The dominant photodisintegration processes vary, depending on the energy absorbed from the photons in the rest frame of the nuclei (28).

$$\frac{1}{E}\frac{dE}{dt}\bigg|_{eff} = \frac{1}{A}\frac{dA}{dt}\sum_i \frac{i}{A}R_{A,i}(E), \tag{2.5}$$

where $R_{A,i}$ is the rate of emission of i nucleons from a nucleus of mass A (28). This process not only alters the particle's energy but also reduces its atomic number, resulting in the creation of lighter particles.

2.1.4 *Adiabatic fractional energy loss*

Adiabatic fractional energy losses also known as cosmological redshift. Is another energy-loss process that dominates at low energies. It can be described as

$$-\frac{1}{E}\left(\frac{dE}{dt}\right)_{adiabatic} = H_0, \tag{2.6}$$

where H_0 is the Hubble constant (28).

In addition to the energy-loss mechanisms mentioned above, synchrotron radiation can also cause UHECRs to lose energy as they move through magnetic fields. This process occurs when charged UHECRs are deflected by magnetic fields, leading to the emission of electromagnetic radiation. However, compared to other processes, synchrotron radiation is a less significant mechanism of energy loss for UHECRs.

In general, these energy-loss mechanisms can significantly alter the original energy, spectrum, and chemical composition of UHECRs by the time they reach Earth. The complex interplay between these different mechanisms, combined with the uncertainties in the sources and propagation of UHECRs, makes the study of UHECRs a challenging field of research (28).

2.2 Magnetic Fields in the Universe

Magnetic fields are ubiquitous in the universe, and they play an essential role in various astrophysical processes, including the propagation of cosmic rays. Since cosmic rays are charged particles, they are subject to magnetic fields such that they are deflected by the Lorentz force.

Larmor radius r_L, which describes the radius of the circular path of a charged particle in a magnetic field, can be calculated by taking into account the particle's charge

Z, energy E, and the strength of the magnetic field B. The formula for the Larmor radius is given as

$$\left(\frac{r_L}{\text{pc}}\right) = 1.1\left(\frac{E}{\text{PeV}}\right)\left(\frac{\mu G}{B}\right)\frac{1}{Z}. \tag{2.7}$$

As already mentioned, there exist GMFs and EGMFs. Although the strength of GMF can be estimated from multiple measurements, the origin and strength of EGMF are not well understood, and its predictions vary considerably (29)(28).

2.2.1 Galactic Magnetic Field

The complex magnetic field present in the Milky Way is not exclusive to our Galaxy and can also be found in the interstellar and intercluster mediums, extending beyond the Galactic disks. These magnetic fields play a crucial role in various astrophysical phenomena, including guiding the motion of cosmic rays and shaping the formation and evolution of stars (30). Moreover, the magnetic field contributes to the total pressure in the Galaxy (31).

The origin of GMF is still not fully understood, but it is believed to be related to the dynamo effect, which generates magnetic fields through the motion of charged particles in a rotating conducting fluid (31). In the case of the Milky Way, which is a spiral galaxy, it is believed that the large-scale magnetic fields observed are amplified and maintained by the dynamo effect, which is thought to be driven by the combined action of differential rotation ω and helical turbulence α (30).

In contrast, slowly rotating systems, such as elliptical galaxies and clusters, exhibit a distinct coherence scale that is smaller than the overall size of the system. This suggests that these magnetic fields could be generated by a more chaotic local, turbulent dynamo where, in the absence of rapid rotation, the field does not organise on large scales (29). In itself, the dynamo paradigm must be considered incomplete, since it does not explain the origin of the initial fields that act as seeds for subsequent dynamo action (29).

The strength of GMF depends strongly on the type of the Galaxy, which implies whether the Galaxy has active dynamos (and thus large-scale magnetic fields) or not and since the probability of containing a large-scale magnetic field depends on the mass of the Galaxy, meaning that the mass of a Galaxy is also a factor (32). For spiral galaxies the total magnetic field is about 10 μG, and then for the same galaxies, but with high star formation rates, it is about (20 - 30) μG. The strongest magnetic fields can then have magnitudes from 50 up to 300 μG, for example Messier 82 (32). There are several ways to measure and quantify the strength of GMF.

Synchrotron Radiation: This is one of the most widely used methods for measuring the GMF in objects ranging from pulsars to superclusters. Synchrotron radiation is produced by high-energy electrons spiraling around magnetic field lines, and the intensity and polarisation of the radiation can be used to map the strength and structure of the magnetic field (32)(29).

Faraday Rotation: This method involves measuring the rotation of the plane of polarisation of the linearly polarised wave as it passes through the magnetic field. The amount of rotation depends on the difference in phase velocities of the right-circularly and left-circularly polarised waves. The change in the polarised angle which refers to the orientation of the plane perpendicular to the direction of a propagating electromagnetic wave, is linearly proportional to the square of wavelength

$$\varphi = \varphi_0 + (RM)\lambda^2, \tag{2.8}$$

where λ is the wavelength of the radiation, φ_0 is the initial polarization angle and RM is the rotation measure that can be obtained from

$$RM = \frac{e^3}{2\pi m_e^2 c^4} \int_0^{l_s} n_e(l) B_\parallel(l) dl, \tag{2.9}$$

where $B_\parallel$ is the parallel component of the magnetic field. As l goes from the observer to the source and m_e is the mass of an electron, $n_e(l)$ being the density of thermal electrons along the line of sight from the source (29).

Zeeman Effect: This method involves measuring the splitting of spectral lines which has normally levels of an atom that are independent of any direction of its angular momentum vectors. This degeneracy is lifted in the presence of a magnetic field by introducing a particular direction into the system, causing the very famous Zeeman splitting. Its the most direct method available for observing magnetic fields since once the ΔE[1] is measured, B can be determined. Providing a measure of the strength of the magnetic field in a given region of the Galaxy (29)(32).

Gamma-Ray Observations: Gamma-ray telescopes can detect gamma rays produced when cosmic rays interact with the GMF, providing a measure of the GMF's strength and structure (33).

As already mentioned it is extremely difficult to accurately determine the true nature of the GMF, leading to the development of various GMF models where some models consider the magnetic effects of the galactic halo to be minor compared to the rest of the Galaxy, while others consider the halo to be a significant contributor to the overall magnetic field. In this study, the Jansson-Farrar 2012 (JF12) model is used (3), which is one of the commonly used models of GMF model in the astroparticle community.

Jansson-Farrar GMF model

First introduced in 2012 by Jansson and Farrar(3). This model is based on a combination of observational data and theoretical calculations and offers a comprehensive framework for understanding the GMF.

It is based on the assumption that the Galactic Magnetic Field (GMF) can be decomposed into two components: a large-scale component, which represents the regular field across large features, and a smaller-scale turbulent component arising

---

[1]the difference in energies

from objects like supernovae. By employing a Bayesian statistical approach and incorporating observational data from various sources, including Faraday rotation RM values from multiple sources to form RM-pixels[2], along with synchrotron emission data, will result in the JF12 model see Figure: 2.1.

First, the **(large-scale)** regular component, which is assumed to be axisymmetric and toroidal in shape, is further decomposed into three separate components. Considered a disk component, which is predominantly located in the plane of the Galaxy and is responsible for the majority of the GMF's strength in this region. The disk component is modelled after the generalised form of the Brown model (34).

The second component is the halo component, which extends above and below the Galactic disk and is responsible for the GMF's strength in the halo region. Several forms of this field are considered, including the axisymmetric and bisymmetric spirals, but the purely toroidal model held the superior fit to the data.

The third component is the X-shaped component, which has a unique structure that is aligned with the X-shaped bulge of the Galaxy. The X-shaped component is modelled as axisymmetric and poloidal, i.e., without any azimuthal component (which is incorporated via the toroidal halo component). It is defined with random orientation and strength on small scales, but its relative magnitude is the same throughout the Galaxy (35).

The **(smaller-scale)** turbulent component is modeled as random field. This turbulent component is thought to arise from the amplification of small-scale magnetic fields by turbulence in the interstellar medium (35).

2.2.2 Extragalactic Magnetic Fields

Magnetic fields exist beyond the confines of individual galaxies. The principles underlying the measurement of EGMFs are similar to those used to study GMF. However, as already mentioned, the task of studying EGMF is considerably more challenging due to the vast distances involved and the much larger space that needs to be explored. The most successful measure of EGMFs comes from the measurement of the Faraday rotation of the few Galaxy clusters, which were within some reasonable range. The strength of magnetic field in Galaxy clusters, with the strongest EGMFs observed reporting strengths of up to several microgauss around the range of $0.1\mu G$ and $1\mu G$ (36). As its visible, these magnitudes are on different scales compared to the GMF, as they are much weaker.

The origin of EGMF is a topic of active research. Several theories have been proposed to explain the origin and evolution of these fields, although none have yet been conclusively proven. Some of the most prominent theories are

Primordial magnetic fields which talks about the existence of magnetic fields in the early universe, which were generated by various processes such as cosmic inflation or phase transitions. These fields were subsequently amplified by gravitational collapse and other processes during the formation of structures, leading to the

---

[2]This process yields a data structure analogous to the synchrotron emission dataset.

EGMF we observe today (37).

Exotic particles and interactions which propose the existence of new particles or interactions beyond the standard model of particle physics, which could generate or modify magnetic fields in the universe. The idea behind this theory is that axion-like dark matter particles could decay into photons and produce magnetic fields in the extragalactic medium (38).

It is important to note that these studies are highly speculative and none have yet been conclusively proven.
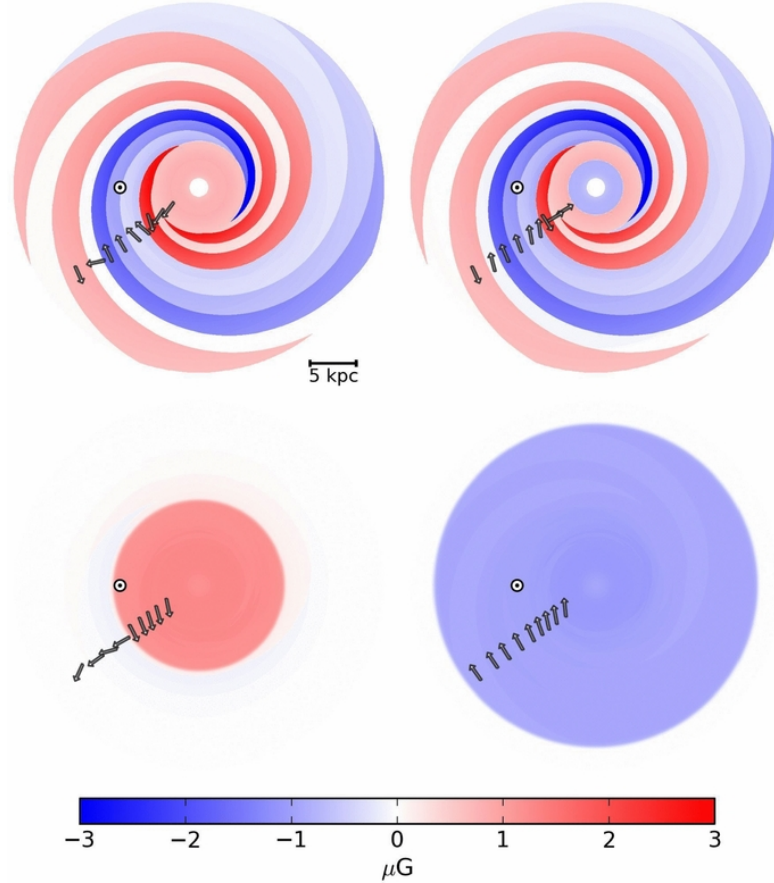
Figure 2.1: Top view of slices in the $x - y$ plane of the JF12 GMF mode model. Top row, from left, slices at $z = 10$ pc and $z =$ -10 pc. Bottom row, slices at $z = 1$ kpc and $z =$ -1 kpc, respectively. The color scheme shows the magnitude of the total regular field, with negative values of the azimuthal component is oriented clockwise. The location of the Solar system is marked with a circle (3).

Chapter 3

The Pierre Auger Observatory

Pierre Auger Observatory, today a state-of-the-art facility that is still undergoing updates for future experiments. It was initially "proposed during the International Cosmic Ray Conference in Dublin in 1991 by Jim Cronin of the University of Chicago and Alan Watson of the University of Leeds"(4). They proposed this facility with a single goal. To investigate and understood cosmic rays of the highest energies. It all came together through a unique partnership of 18 countries, which pushed toward first constructions back in 2000 and was finished in 2008; however, first data collection started during the construction in January 2004 with 154 active detector stations. The first physics results were then presented during the 2005 summer conference (4) (39).

For the construction, it was important to choose the right location with sufficient area to host such a large experiment, as it had become clear that only a very large array would yield high statistical power to cover almost complete sky, which is necessary for the observation of the highest-energy cosmic rays. On the basis of these conditions, the province of Mendoza, located in Argentina, was chosen. It provided a generally flat area for which the detectors would be located at altitudes between 1340 and 1610 m. This allows for the network of 1660 Surface Detectors (SD) placed in regular triangular patterns with a spacing of 1500 m with a total area of approximately 3000 km^2 resulting in overall sensitivity for cosmic rays above 10^{18} eV. There also exists a smaller array of SD stations positioned within the overall array with a smaller array separation of 750 m between each SD detector. It was one of the Pierre Augers Observatory updates called AMIGA (Auger Muon and Infilled Ground Array), which aimed to extend the sensitivity up to 10^{17} eV, which allowed for the detection of less energetic cosmic rays. This is then surrounded with four fluorescence detectors (FD), see Figure: 3.1 which shows detector positions where each red dot represents one SD station and the FD stations then surround the perimeter of the whole array, namely; Los Leones, Los Morados, Loma Amarilla, and Coihueco, together with its view direction visualised in green line. See Figure: 3.4 for a visual representation of the FD and SD detectors.

The final design is a unique facility that uses two different types of detector to study cosmic-ray showers: The SD continuously records the particle densities as cosmic-ray showers hit the ground, and the FD measures the longitudinal development of the

showers by detecting the amount of nitrogen fluorescence light produced along its path as a nearly calorimetric detector, allowing precise measurements of energy. SD offers an almost 100% duty cycle, while FD can only operate on dark and moonless nights which therefore has a duty cycle of around 15%.

An essential feature of Auger is its hybrid design. Observing showers simultaneously using two different but complementary techniques and combining them allows for a precise determination of the position of a shower axis in the atmosphere with an accuracy better than that that could be achieved independently with either the SD or FD (4).
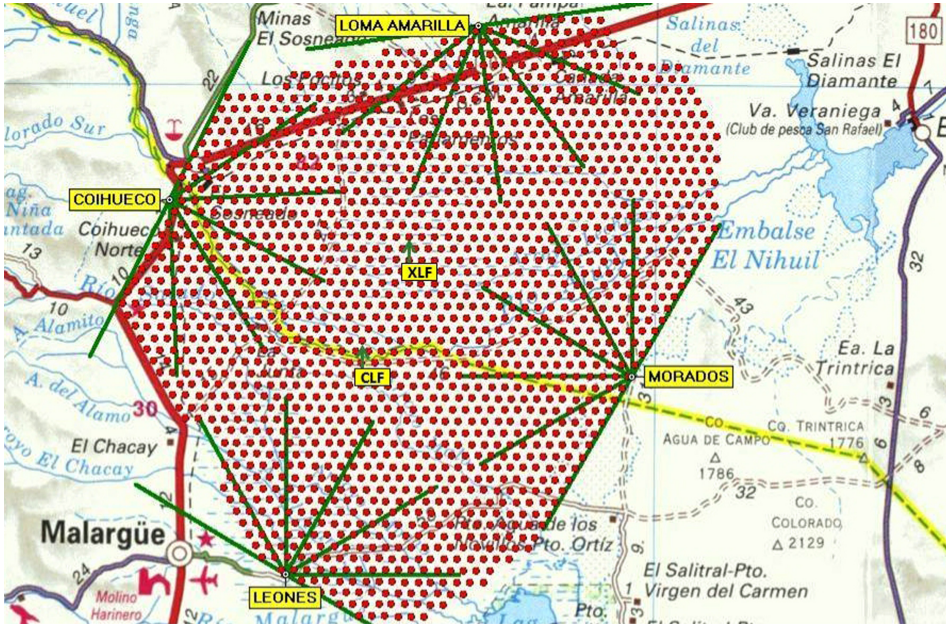
Figure 3.1: Detector layout of the Pierre Auger Observatory. Each red dot represents one SD station. The four FD sites, labelled yellow, are also shown with an indicated field of view (green) for each of the individual telescopes (4).

3.1 Surface Detectors

Surface detector is a water Cherenkov detector with fully autonomous cylindrical tanks, with dimensions of 3.6 metres in diameter and a maximum height of 1.6 metres, the schematic of the SD detector can be shown in Figure 3.2. The inner surface is entirely reflective and sealed with a specialised liner, enabling it to hold 12,000 litres of ultra-pure water that prevents bacterial growth, which could otherwise compromise water clarity. Equidistantly placed on the liner's surface are three Photonis XP1805/D1 photomultiplier tubes (PMTs), each with a diameter of 9 inches. These PMTs are situated in such a way as to minimise the impact of the geomagnetic field, with their orientation aligned with the azimuth of Earth's magnetic field (4).

When relativistic charged particles or high-energy photons traverse the water at a speed greater than the speed of light in that medium, it polarises the nearby

atoms, which generate Cherenkov light that is subsequently registered as a signal by the photomultipliers. This signal is quantified in units of Vertical Equivalent Muon (VEM)[1]. However, prior to any energy reconstruction or additional calculations, the SD detector requires calibration to accurately measure the value of 1 VEM. During shower reconstruction, the recorded signal is converted to VEM, and the total shower energy and arrival direction are determined using a lateral distribution function from FD stations. This process is further elaborated upon in hybrid reconstruction, as neither SD nor FD are utilised independently.

Each SD station is also equipped with a GPS receiver and data acquisition system used to record the detection time in each SD, which is then synchronised across each SD station to determine where the shower was detected first. In addition, an accompanying radio transceiver and power controller are included, as well as a control function that allows remote operation (4).

These SD stations not only exhibit exceptional geometry and sensitivity within the experiment, but also demonstrate reliability, minimal maintenance requirements, and cost-effectiveness. Such durable solar powered equipment with a duty cycle of nearly 100% is ideally suited for the prevailing environmental conditions (4).
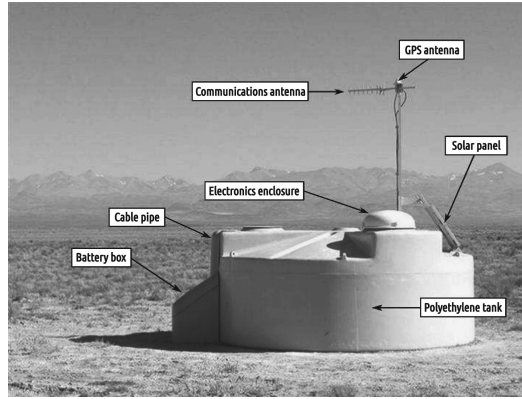
Figure 3.2: A schematic view of a surface detector station in the field, showing its main components (4).

3.2 Fluorescence Detectors

In total, there are 27 FD telescopes from four distinct sites. Each FD station houses six independent telescopes located within clean, climate-controlled buildings. These telescopes have a field of view of 30 ° x 30 ° in azimuth and elevation, providing a cumulative coverage of 180 ° in azimuth (4).

The telescope design is based on Schmidt optics, which reduce coma aberration, while an annular lens further eliminates it and corrects for spherical aberration. The schematics of such a telescope are illustrated in Figure: 3.3. Fluorescence light, emitted by an air shower, enters through a circular diaphragm with a radius of 1.1

---

[1]A signal produced by a muon traversing the tank on a vertical trajectory.

metres (4). Positioned behind a Schott MUG-6 filter glass window, this diaphragm serves as a UV spectrum filter, allowing between 50 and 80 % of UV light to pass through. It is crucial to note that these percentages are based on light wavelengths ranging from 310 to 390 nm. The minimal UV losses yield a substantial reduction in other background light fluxes, thereby enhancing the signal-to-noise ratio. The diminished light subsequently falls onto a hexagonal or rectangular segmented spherical mirror with a radius of 3,400 mm and is then focused onto a camera equipped with photomultipliers (40).

As previously stated, FD stations have a duty cycle of approximately 15% due to not being able to operate in daylight, in addition conditions such as bad weather or high flux from moonlight also reduce this duty cycle. To prevent potential damage to the detectors, the stations are equipped with shutters that close during daylight hours and automatically shut at night when the wind speeds increase or rainfall is detected. Additionally, a fail-safe curtain is mounted in the background. All FD telescopes are then remotely operated by shift personnel from the central campus.

As mentioned earlier, the FD stations measure the longitudinal profile, which is utilised in conjunction with SD in hybrid reconstruction. Further details on this process are provided in the following section.
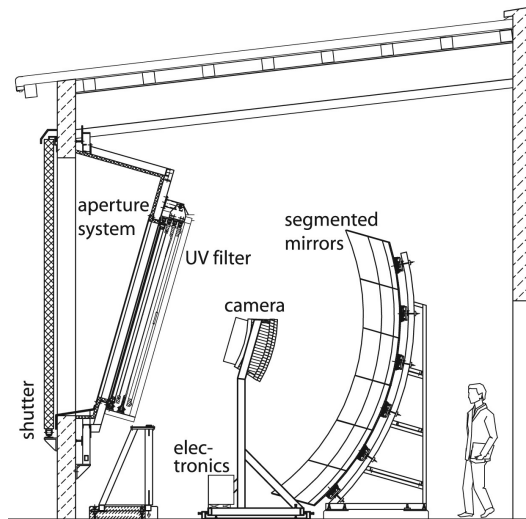
Figure 3.3: Schematic view of a fluorescence telescope with a description of its main components (4).

3.3   Hybrid Reconstruction

As indicated above, a key feature of the Pierre Auger Observatory is its hybrid design, which allows the measurement of properties of primary cosmic rays by using different techniques for which we have different varying systematic uncertainties. For the reconstruction, the data of both FD with additional timing information from the SD are exploited such that the amplitude and timing of the signals detected by each PMT in each telescope as well as additional timing information from the SD

station with the highest signal. Results in improved directional precision. Such precise geometry of the hybrid event is the first step toward high-quality measurements of the longitudinal profile of the shower, which, in turn, yields the energy of the primary particle and the depth of maximum X_{max} with statistical resolutions for a single site of approx 10% and 20 g/cm^2 for energy and X_{max} respectively, at around 10^{19} eV (41) (42) (4).

An additional example of the synergy between the two techniques can be shown in a situation where showers arriving with zenith angles less than 60° will under normal conditions provide better exposure when only SD is involved. However, the surface array presents a challenge when trying to correlate the primary energy with a specific observable, such as the signal measured by the water Cherenkov detectors located 1,000m from the shower axis S(1000)^2, which can only be found using cascade simulations. This is a problem as this method is unreliable since the hadronic physics for such energies is unknown and, therefore, impractical to assign systematic uncertainty. Here, using the hybrid system provided an alternative method which is essentially free from using simulations (the reason why not completely free is due to the small fraction approx. 10% that goes into neutrinos and high-energy muons that continue into the ground) (4).

Figure 3.4: Los Leones fluorescence detector enclosure (top) and surface detector station (bottom) (4).

---

^{2}Total signal at a core distance of 1000 m.

Chapter 4

Physics Motivation for mass-dependent anisotropy studies

The primary motivation for this project stems from the substantial contributions made by the Pierre Auger Observatory (Auger) in advancing our understanding of the mass composition of cosmic rays that arrive on Earth.

In 2016, the observatory published a study (7) that provided evidence for a mixed mass composition of cosmic rays at the ankle in the energy spectrum . Such is a feature that might mark the transition between galactic and extragalactic cosmic rays, which can be observe slightly above energies of 8 EeV, as is shown in Figure: 4.1, which illustrates Auger's observed energy spectrum based on collected data.
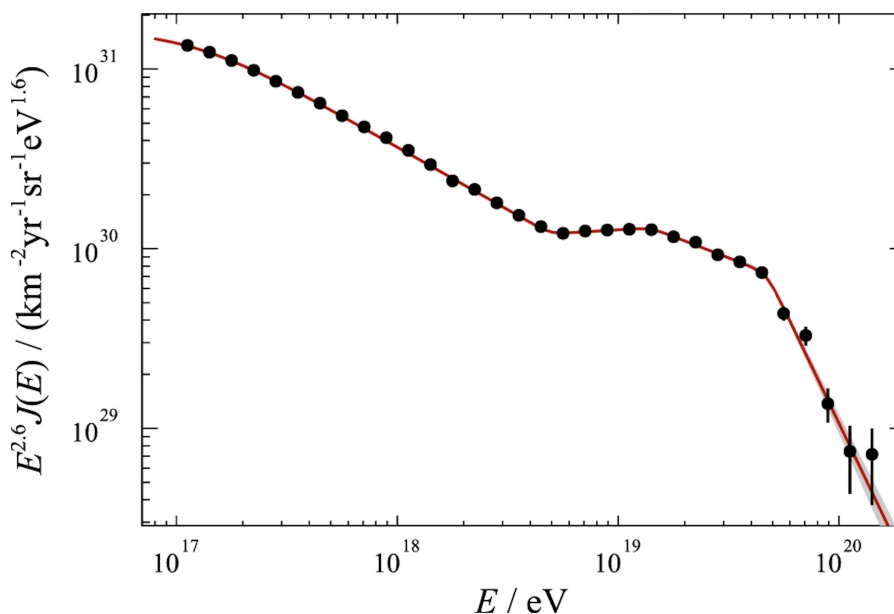
Figure 4.1: SD energy spectrum after combining individual measurements with the SD-750 and SD-1500 scaled by $E^{2.6}$. The fit using the proposed function labeled as (Eq. (9) in (5)) is overlaid in red along with the one-sigma error band in gray which represent statistical uncertainties. Taken from (6).

Another important discovery was observed in the "ankle" region which can be see in Figure: 4.2. The goal of these figures was to investigate the relationship between X_{max} and the ground signal detected in air showers. This was then used to observe a correlation of the ranking coefficient r_G which was introduced by Gideon and Hollister (43), it determinate whether the composition of the cosmic-ray mass is pure or mixed (7).

In simulations, it's observed that pure cosmic-ray mass compositions typically exhibit r_G correlation coefficient close to or greater than zero. However, in the case of mixed mass compositions, a negative correlation would be observed. From the obtained data by the two independent detection techniques, first is the FD for X_{max} second is the S(1000) which has significant sensitivity to muons, therefore both SD and FD was used to eliminate any systematic correlated detector bias. Since both the S(1000) and X_{max} depends on shower energy and in case of the S(1000) also on the zenith angle, therefore, S(1000) and X_{max} are scaled to a reference energy of 10 EeV and a zenith angle of 38°, denoting these scaled quantities as X_{max}^{*} and S_{38}^{*} (7).

The reason why this ranking coefficient was chosen is due to its insurance against any modifications leaving the ranks of events unchanged (in particular to systematic shifts in the observables). The primary differentiation between this particular ranking coefficient and others lies in the fact that the rank values themselves are not used directly in the calculations, thereby establishing a unique approach. Where a rather then the general statistical dependence between X_{max}^{*} and S_{38}^{*} is estimated by counting the difference in numbers of events with ranks deviating from the expectations for perfect correlation and anti-correlation (7).

The resulting correlation value observed is then $r_G = -0.125 \pm 0.024$ of measured data indicates that particles at such energies consist of a mixed mass composition (7).
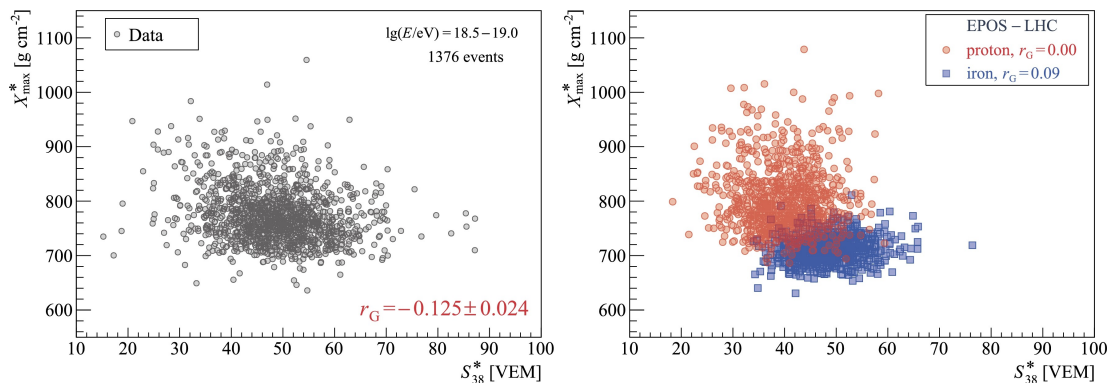
Figure 4.2: Left: measured distribution of X_{max} vs. ground signal S_{38}, both corrected for energy evolution, for $lg(E/eV) = 18.5$ -19.0. Right: the same distribution for 1000 proton and 1000 iron showers simulated with EPOS-LHC. Taken from (7).

In 2018, the Auger collaborations made one of the most significant discoveries, demonstrating the significance $> 6\sigma$ of a large-scale dipole anisotropy above 8 EeV (44). This discovery revealed that only the dipolar components are statistically significant and that the dipole is positioned $\approx -125°$ away from the Galactic centre, as seen in Figure: 4.3, which further supports the extragalactic origins of cosmic rays.
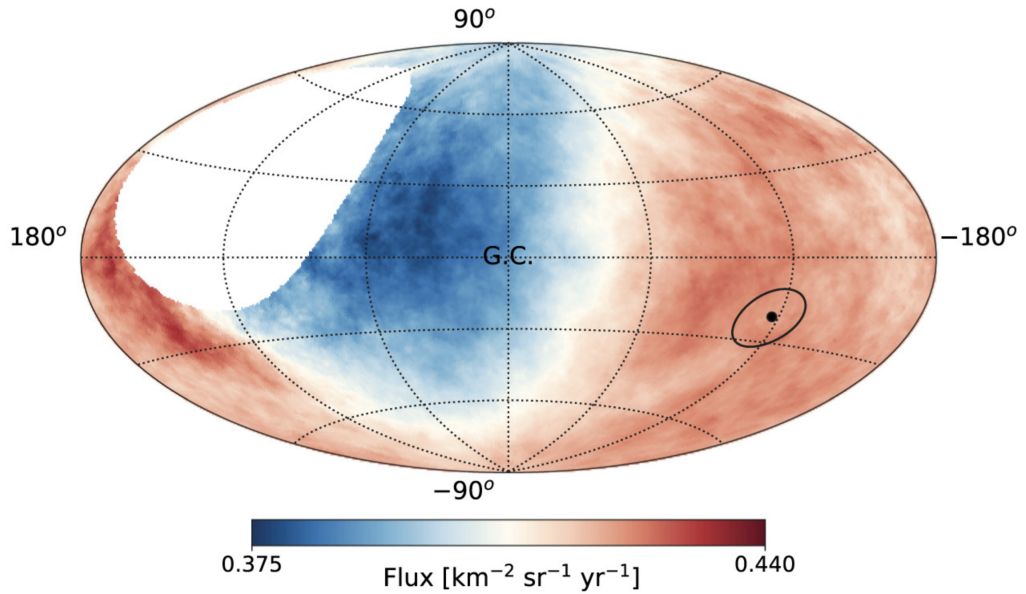
Figure 4.3: showing the cosmic-ray flux detected by the Pierre Auger Observatory above 8 EeV, in Galactic coordinates, smoothed with a 45° top-hat function (the Galactic Centre, GC, is at the origin). The dot indicates the measured dipole direction and the contour denotes the region of the confidence level 68% from (8).

Another study that followed was more specified on the compositions of the arrival particles as its shown in Figure: 4.4, it is suggested per (9) that the mean mass of primary particles that arrive from the on-plane whose are defined as particles within $\pm$ 30° from the galactic plane (using galactic latitude), region is greater than that of those that come from the off-plane region represent by all the other arrival directions. The following Figure: 4.5 shows then a comprehensive map of this observations results, in conclusion its visible that where particles measured from the plane exhibit a heavier mean mass.
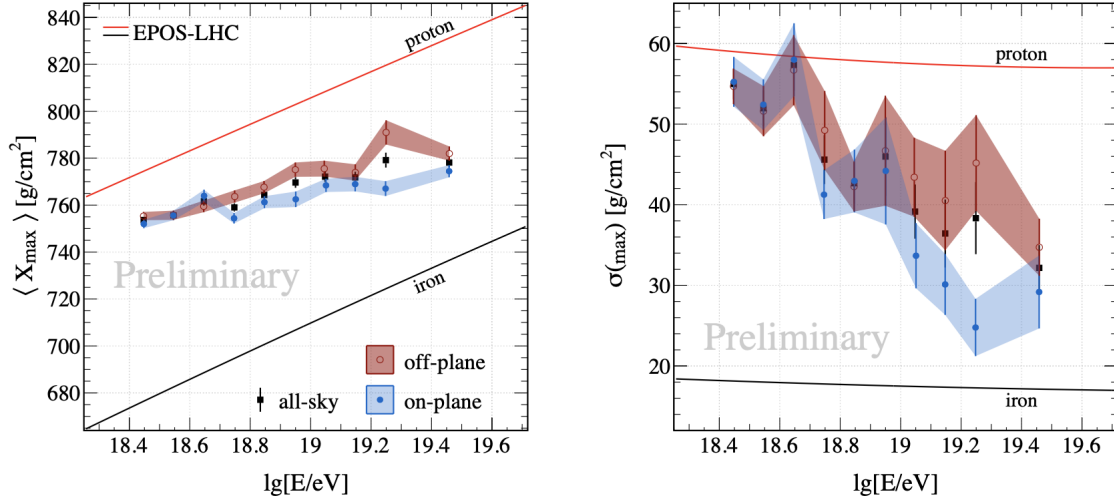
Figure 4.4: The X_{max} moments of the on-off-plane regions. Taken from (9).
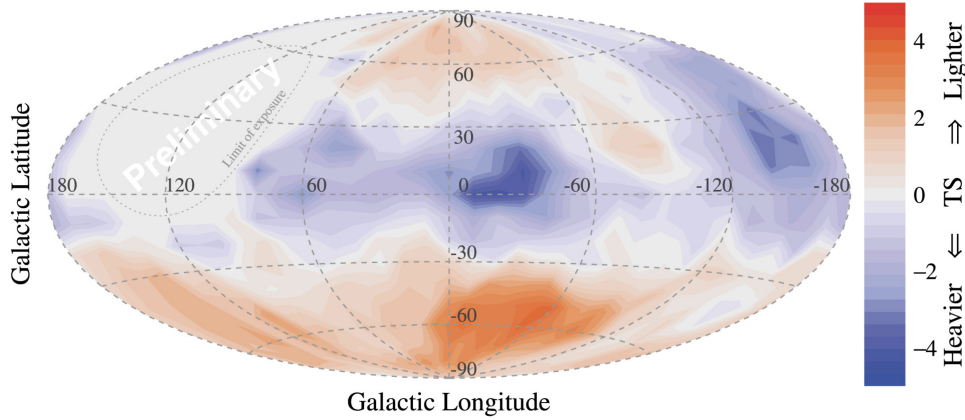
Figure 4.5: Sky map of comic-ray composition for E greater than $10^{18.7}$ eV. Taken from (9).

All the mentioned observations piqued curiosity and served as the driving force behind this diploma thesis, with the aim of answering questions regarding the compositions, its effect on GMF and specific mixes that could cause such anisotropies, in addition we will analyse to what degree does the the dipole distribution of extragalactic dipoles plays a significant role in this scenario. Hence in the following chapters we will describe the main framework and approach for how to simulate particles for use in the following analysis, after which the results for 3 different cases will be presented.

Chapter 5

Cosmic ray simulations

In the following section, we introduce the simulation setup for generating particles and the various methods used to reweight the simulated data. The end point was to produce data that closely approximate real observable conditions.

5.1 Simulation of cosmic ray propagation

To simulate particles which would consider GMF for multiple elements, an open framework simulation called CRPropa 3 is used. It is a publicly available software written in C++ and can be imported in form of library into Python 3. It is a modular structure as shown in Figure: 5.1, each module has functions as a list of classes that can be used (10).

The initial setup involved modules such as a three-dimensional mode of CRPropa 3, which propagates particles in three dimensions. Following by the addition of the magnetic fields for which CRPropa offers both GMF and EGMF, however this project focuses on observing particles within the galaxy, therefore, only the GMF and its corresponding JF12 model (see Section: 2.2.1) is used. Due to the propagation in relatively short distances energy losses can be neglected (see Chapter 2.1).

The observer is defined as a sphere with a 20 kpc radius, and it is also defined as the source. This allowed us to use the CRPropa for so called **Back-tracking:**, which is a general method that considers the observer as a starting point and propagate particles isotropically away from this point-like source, with opposite charges acting as antiparticles. In our case the particles are propagated towards the edge of the Galaxy. The advantage of this approach is that it significantly reduces computational time, as all particles are included in the final output. The validity of this approach can be demonstrated in the Appendix: .2, where its compared to a forward-tracking method obtained by the author of (12) which generates the particle at the edge of the galaxy and propagates then towards the observer. Both methods produced equivalent results. Therefore, the less time-consuming backtracking method was chosen to propagate 1,000,000 individual proton, helium, nitrogen, and iron nuclei through the GMF. The energy spectra followed a power law E^{-1} and spanned energy range

from 3.15 EeV to 100 EeV. The Python code used in the analysis can be found in the appendix: .1.
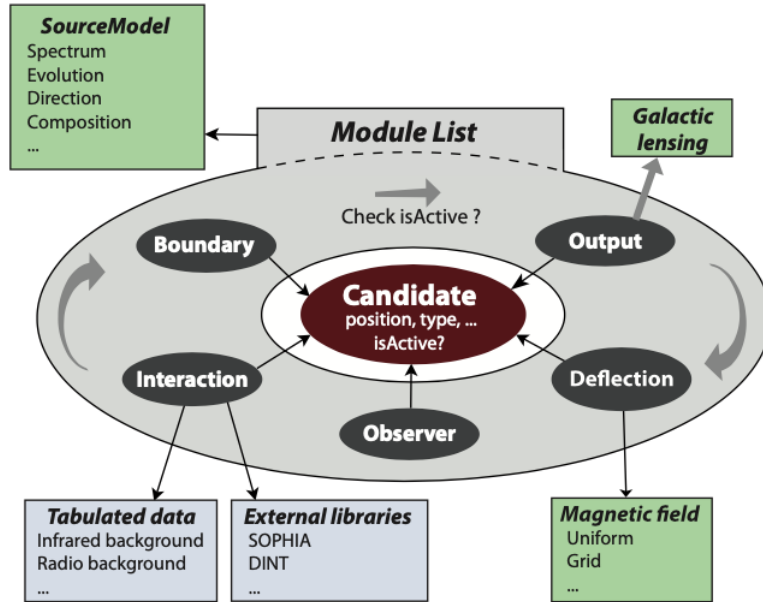
Figure 5.1: Illustration of the modular structure of CRPropa 3. Each module contained in the module list acts on the candidate class (10).

5.2 Estimation of FD exposure

Real Monte Carlo simulations (45) were used as a mean to estimate the FD exposure. It is a tailored Monte Carlo approach that is designed to closely emulate realistic scenarios and incorporates details about the detectors to adjust the simulated data to match the real-life observations. To be more precise, the Offline v3r3p4-icrc2017-preprod-v3 which is a general purpose framework which allows collaborators to contribute algorithms and sequencing instructions to build up the variety of applications (46). It consists of three distinct hadronic interaction models, namely QGSJet II-04, EPOS-LHC (using CONEX 5.40) and Sibyll 2.3c (CONEX 5.64) where CONEX is a hybrid simulation code that is suited for fast one-dimensional simulations of shower profiles (47). These hadronic models cover a range of energies from 0.4 to 158 EeV. The simulated energies are then corrected to correspond to the observed energy spectrum (5) as the spectral index of generated energy spectra was 1.75, similarly to our simulations done in CRPropa 3. The simulated showers are then passed through series of high-quality selections for X_{max} analysis (44) and applying an energy selection between 5 and 100 EeV. Only after this are the Monte Carlo simulated particles plotted and used as a look up map to estimate the FD exposure; see Figure: 5.2.
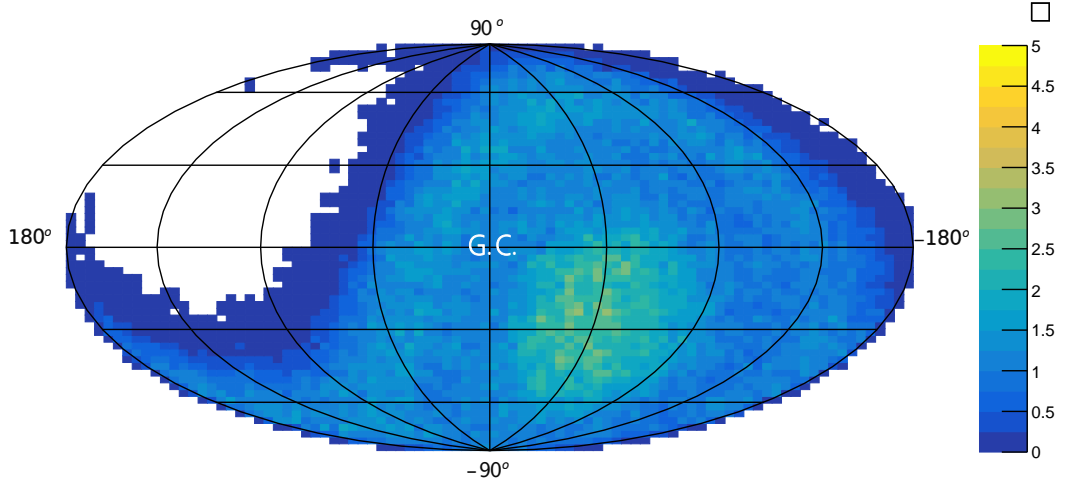
Figure 5.2: The exposure of FD of the Pierre Auger Observatory obtained from real MC simulations in galactic coordinates.

5.3   Correction factors

To achieve data that resemble real-world conditions observed at the Pierre Auger Observatory, multiple weights are applied to the particles generated by CRPropa 3. In this section each of the applied weight is described.

Dipole: representing the first weight. Its calculated by the following equation:

$$W_1 = \text{AP} \cdot \cos(\delta) + 1.0$$

where "AP" is the amplitude of the dipole and δ represents the angular distance between the initial direction of the simulated particle and the direction of a dipole. Is defined as follows:

$$\delta = \arccos\left[\sin(\text{b}_\text{D}) \cdot \sin(\text{b}_\text{In}) + \cos(\text{b}_\text{D}) \cdot \cos(\text{b}_\text{In}) \cdot \cos(\text{l}_\text{D} - \text{l}_\text{In})\right],$$

where the "b_D", "l_D" are the positional coordinates of the dipole in galactic coordinates. The other variables "b_In", "l_In" are the initial latitude and longitude of the simulated particle.

FD exposure: The W_2 which represent the second weight that is obtained from the real MC simulations described in previous section by the utilisation of ROOT's (48) functions FindBin and GetBinContent.

Correction for energy spectrum: Third weight that corrects the spectrum E^{-1} above the ankle and below the ankle, see Figure: 5.3 and Figure: 5.4 which represent the before and after correction. If the energy is bellow the ankle then only the following correction is applied :

$$W_3' = 10^{(\text{E} - \text{E}_\text{min}) \cdot (\alpha - \Gamma)}.$$

If the energy is above the ankle, then the previous correction is still applied but there will be additional correction on top of it:

$$W_3 = W_3' \cdot 10^{(\text{E}-\log(\text{E}_\text{a}))\cdot(\Gamma_1-\Gamma_2)}.$$

Where E is the energy of the simulated particle, $E_{min} = 18.7$ in the units of $\log(\text{E}_{min}/\text{eV})$ is the chosen minimum energy, $\alpha = 1.0$ is the Spectral Index for real MC, also in the units of $\log(\text{E}_\text{a}/\text{eV})) = 18.7$ which is the point at which the ankle is located. Then $\Gamma_1 = 3.29$ for the below ankle and $\Gamma_2 = 2.51$ for the above ankle.
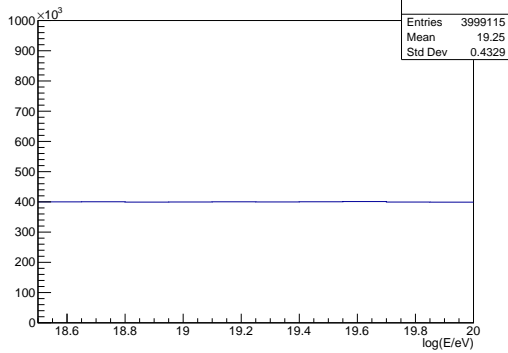
Figure 5.3: Before applying the correction for energy spectrum (W_3) to the simulated energy spectrum of CRP.
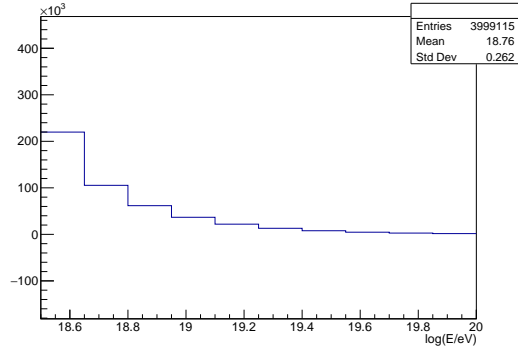
Figure 5.4: After the applying the correction for energy spectrum (W_3) to the simulated energy spectrum of CRP.

The weights are then multiply into single values that will be used as a total correction factor for each simulated particle during the analysis.

5.4 Generating X_{max}

For each simulated particle which passes the corrections mentioned in previous section, the X_{max} values is generated. This is done using a generalised Gumbel distribution, which is a probability distribution often used in extreme value theory, since UHECR are extreme event therefore this distribution is a good fit for the analysis (49).

To successfully calculate X_{max} the generalised Gumble has a form;

$$G(\mu, \sigma, \lambda) = \lambda^{\lambda} * e^{\frac{-\lambda(x-\mu)}{\mu} - \lambda e^{\frac{-(x-\mu)}{\sigma}}}.$$

Which requires three parameters;

$$\mu(A, E) = p_{0u} + p_{1u} \log_{10}(\frac{E}{E_0}) + p_{2u} \log_{10}^2(\frac{E}{E_0}),$$

$$\sigma(A, E) = p_{0\sigma} + p_{1\sigma} \log_{10}(\frac{E}{E_0}),$$

$$\lambda(A, E) = p_{0\lambda} + p_{1\lambda} \log_{10}(\frac{E}{E_0}).$$

The μ, σ, λ, parameters have been parameterized as a function of energy, nuclear mass, and some constants which can be obtained from EPOS-LHC model (50).

Chapter 6

Mass-dependent anisotropy as a consequence of Galactic magnetic field using on-off Galactic plane selection

In this chapter, we examine the effects of the Galactic Magnetic Field (GMF) on the mass-dependent anisotropy in the arrival directions of particles above $10^{18.7}$ eV, motivated by recent observations (9) which were described in detail in Chapter 4. To investigate the origin of this effect, four types of particles were propagated in GMF using the CRPropa 3 simulation (see Section 5.3). The simulated particles are then divided according to their arrival direction, which is determined by the on-off galactic plane, as per (9). Particles within $\pm$ 30° from the galactic plane in galactic latitude are classified as originating from the on-galactic plane, while the remaining particles are considered to be from the off-galactic plane. The analysis is then carried out for the mixtures of four primary particles (p, He, N, Fe) that are constructed by their division into relative fractions by 10%, resulting in a total of 286 possible combinations.

In the following sections of this chapter, we will first investigate the case of isotropic distribution of the arrival directions of simulated particles entering the Galaxy, from which no significant mass-dependent anisotropies are observed in the $\Delta\langle X_{\max}\rangle$ which is defined as the difference between the mean $X_{\max}$ on-galactic and mean $X_{\max}$ off-galactic plane. This result is expected from the isotropic distribution, leaving the values of the figures in Section 6.1 as a statistical fluctuation. This will be followed by an anisotropic distribution of simulated particles entering the Galaxy for which we then analyse the effect of $\Delta\langle X_{\max}\rangle$ for the on-off galactic plane in relation to $\langle \ln(A)\rangle$ which represents the mean logarithmic mass A of a cosmic-ray mix, where A is the atomic mass number, and $\sigma^2(\ln(A))$ which represents the spread of the mass distribution of primary cosmic rays. The last section includes a specific case for the $\Delta\langle X_{\max}\rangle$ distribution of the on-off galactic plane for a mixture of 50% - 50% proton - iron. All analyses carried out in this chapter did not result in a difference of $\Delta\langle X_{\max}\rangle$ and $\Delta\sigma(X_{\max})$, (see Appendix .4 for $\Delta\sigma(X_{\max})$), which is incompatible

with the observed values of (9.1 ± 1.6) g/cm^2 and (5.9 ± 2.1) g/cm^2 for $\Delta\langle X_{\text{max}}\rangle$ and $\Delta\sigma(X_{\text{max}})$, respectively, as described in (9).

6.1 Isotropic

The following figures represent the isotropic scenario of arrival directions of cosmic rays at the edge of the Galaxy where, for the on-off galactic plane selection, no significant $\Delta\langle X_{\text{max}}\rangle$ was obtained.

In Figure: 6.1 the sky map in galactic coordinates remains isotropic for arrival directions on observer, which reveals a uniform flux throughout, thereby confirming Liouville's theorem, which states that "an anisotropy cannot arise through deflections of an originally isotropic flux by a magnetic field" (11). Figure: 6.2 which represents the relationship between $\Delta\langle X_{\text{max}}\rangle$ and $\langle\ln(A)\rangle$ provides a range of values from the lowest of (-0.3 $\pm$ 0.2) g/cm^2 up to the largest (0.1 $\pm$ 0.2) g/cm^2 with the overall behaviour showing uniform changes of the $\Delta\langle X_{\text{max}}\rangle$ across the mixes with no significant value, which is as expected from an isotropic distribution. Figure: 6.3 represents the relationship between $\Delta\langle X_{\text{max}}\rangle$ and $\sigma^2(ln(A))$ with a values ranging from, lowest of (-0.3 $\pm$ 0.2) g/cm^2 up to the largest (0.1 $\pm$ 0.2) g/cm^2 with the overall behaviour showing a uniform distribution in all compositions with no significant value for any of the mixes, as expected from the isotropic distribution. Last but not least, Figure: 6.4 that explores the $\Delta\langle X_{\text{max}}\rangle$ distribution of the on-off galactic plane for the extreme case represented by the mixture of a 50-50% of protons and iron nuclei, obtaining a $\Delta\langle X_{\text{max}}\rangle$ value of (-0.1 $\pm$ 0.3) g/cm^2.
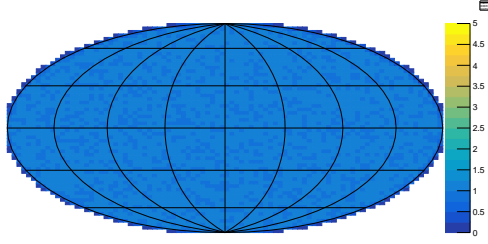
Figure 6.1: Mollweide projection with isotropic distribution of protons in galactic coordinates. Z-axis represent the flux intensity.

Figure 6.2: For energy above $10^{18.7}$ eV all 286 possible mixed compositions of p, He, N and Fe with isotropic distribution of arrival directions to the Galaxy are represented as a plot of $\Delta\langle X_{\max}\rangle$ versus $\langle \ln(A)\rangle$.

Figure 6.3: For energy above $10^{18.7}$ eV all 286 possible mixed compositions of p, He, N and Fe with isotropic distribution of arrival directions to the Galaxy are represented as a plot of $\Delta\langle X_{\max}\rangle$ versus $\sigma^2(\ln(A))$.
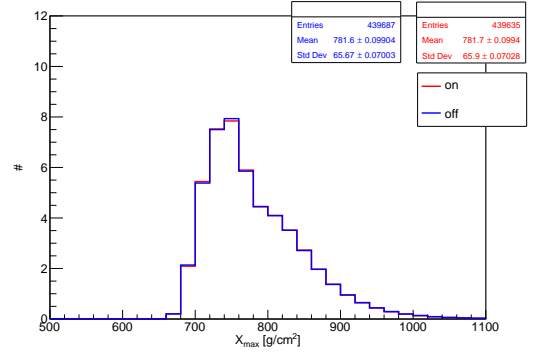
Figure 6.4: On-and off-galactic plane distributions of $X_{\max}$ for isotropic distribution of arrival directions to the Galaxy of 50/50 mix of protons (p) and iron nuclei (Fe) for energy above $10^{18.7}$ eV.

6.2 Anisotropic

The simulated particles with an energy above $10^{18.7}$ eV were chosen according to (9). They were reweighted (see Section 5.3) to closely resemble real-world observations made at the Pierre Auger Observatory (44). In the following analysis, the Auger dipole coordinates are given as $(l, b) = (-127.0°, -13.0°)$ in galactic coordinates with an amplitude of $0.065^{+0.012}_{-0.09}$ (44). However, to achieve amplitudes on the observer similar to those in (44), the amplitude value of the dipole at the edge of the Galaxy was set to 0.08 for all composition mixes.

6.2.1 $\Delta\langle X_{\mathrm{max}}\rangle$ relation with Energy

To study the potential energy dependence or include possible systematic uncertainties in the energy calibration, several energy thresholds were chosen for the analysis in steps of 0.5 in log E. No obvious energy dependence of $\Delta\langle X_{\mathrm{max}}\rangle$ was found; see Figure: 6.5 which represents the extreme value of the case of the relationship between $\Delta\langle X_{\mathrm{max}}\rangle$ for on-off galactic and its corresponding energy thresholds.
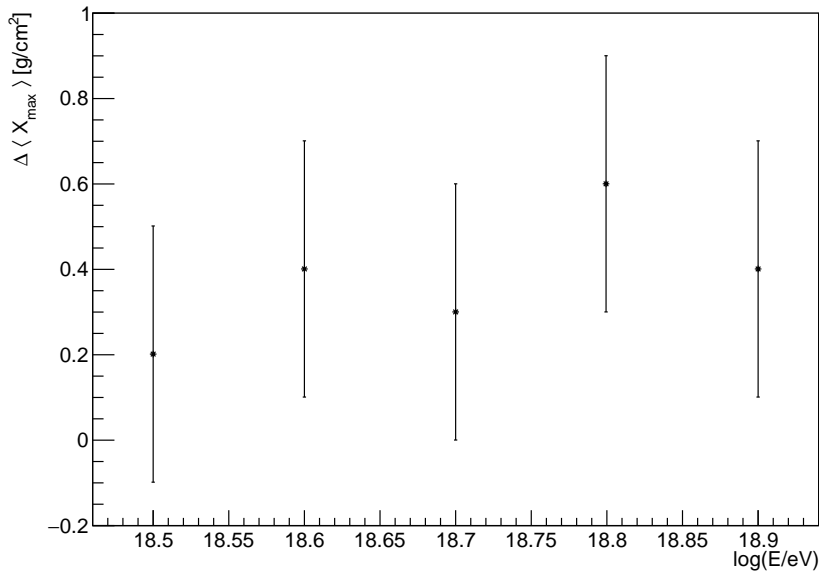
Figure 6.5: $\Delta\langle X_{\mathrm{max}}\rangle$ for on-off galactic plane and its corresponding energy thresholds.

6.2.2 $\Delta\langle X_{\text{max}}\rangle$ vs $\langle \ln(\text{A})\rangle$

In this section for energy above $10^{18.7}$ eV, we obtained values of $\Delta\langle X_{\text{max}}\rangle$ for the on-off Galactic plane, ranges from the minimum of (-0.2 $\pm$0.3) g/cm^2 to a maximum of (0.8 ± 0.3) g/cm^2 see Figure: 6.6. The overall behaviour displays a non-significant $\Delta\langle X_{\text{max}}\rangle$ in comparison to the isotropic figure discussed in Section 6.1. This suggests that there is either no correlation or an insignificant correlation between the size of cosmic ray composition mixing and $\Delta\langle X_{\text{max}}\rangle$ which is in contradiction to the observations in (9).
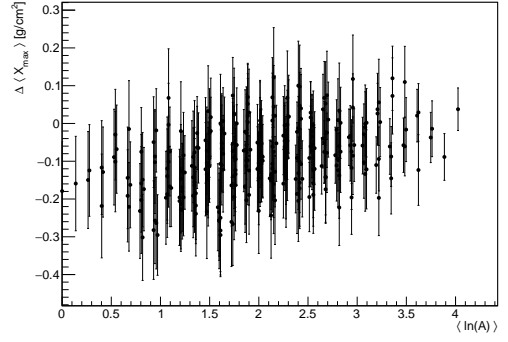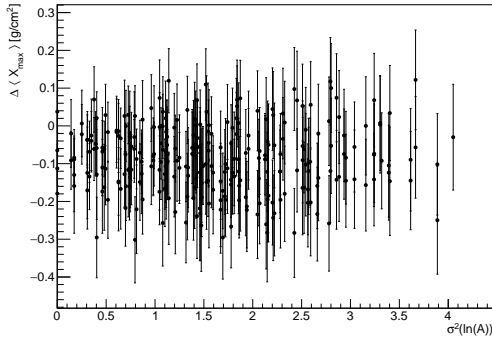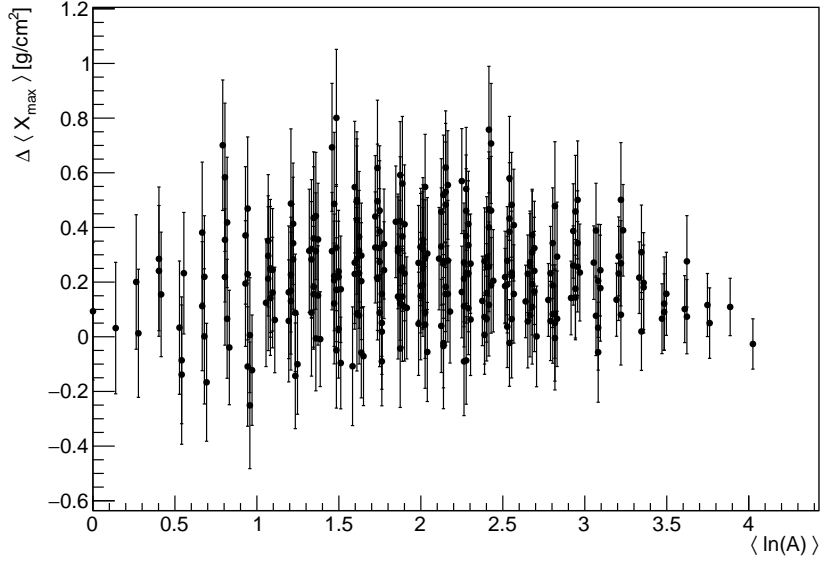

Figure 6.6: For energy above $10^{18.7}$ eV all 286 possible mixed compositions of p, He, N and Fe with anisotropic distribution of arrival directions to the Galaxy are represented as a plot of $\Delta\langle X_{\text{max}}\rangle$ versus $\langle \ln(\text{A})\rangle$.

6.2.3 $\Delta\langle X_{\mathbf{max}}\rangle$ vs $\sigma^2(\mathbf{ln(A)})$

Similarly to the previous section, the $\Delta\langle X_{\max}\rangle$ for the on-off Galactic plane varies from the minimum (-0.2 $\pm$ 0.3) g/cm^2 to the maximum (0.8 $\pm$ 0.3) g/cm^2 value for energies above $10^{18.7}$ eV see Figure: 6.7. The overall behaviour exhibits a non-significant $\Delta\langle X_{\max}\rangle$ value, and its variation dispersion resembles more of a statistical fluctuation observed in isotropic figure discussed in Section 6.1. This implies that there is either no correlation or insignificant correlation between the size of cosmic ray composition mixing and $\Delta\langle X_{\max}\rangle$ value, which contradicts the observations in (9).
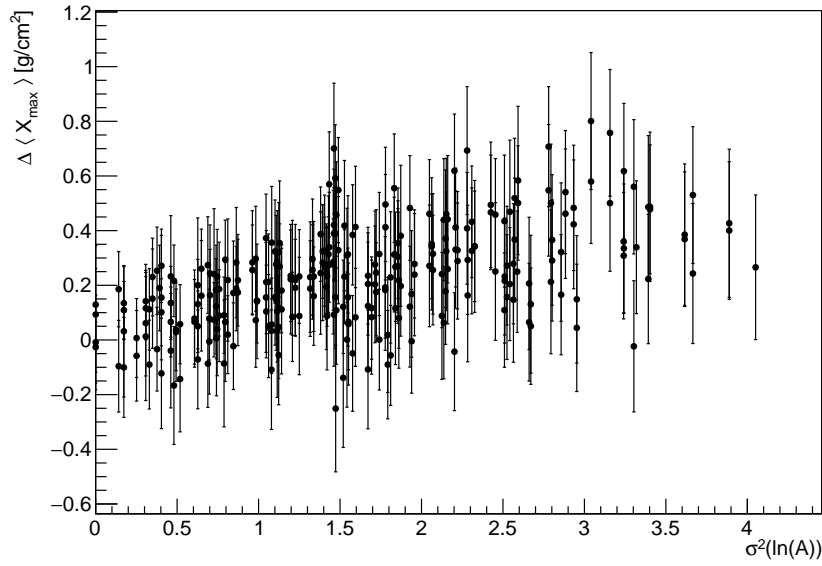
Figure 6.7: For energy above $10^{18.7}$ eV all 286 possible mixed compositions of p, He, N and Fe with anisotropic distribution of arrival directions to the Galaxy are represented as a plot of $\Delta\langle X_{\max}\rangle$ versus $\sigma^2(\ln(A))$.

6.2.4 $\Delta\langle X_{\mathbf{max}}\rangle$ of 50% - 50% proton - iron mix

The highest $\Delta\langle X_{\max}\rangle$ and $\Delta\sigma(X_{\max})$ for the on-off Galactic plane is anticipated in the extreme case depicted in Figure: 6.8, which consists of a mixture of a 50-50% of protons and iron nuclei. A detailed examination of the non-significant values $\Delta\langle X_{\max}\rangle$ and $\Delta\sigma(X_{\max})$ is present in the Table: 6.1, which reveals a closer resemblance to the isotropic figure in Section 6.1 than that depicted in (9).

	Entries	476434	Entries	476299
Mean	758.1 ± 0.1806	Mean	757.8 ± 0.194
Std Dev	65.5 ± 0.1277	Std Dev	65.7 ± 0.1372
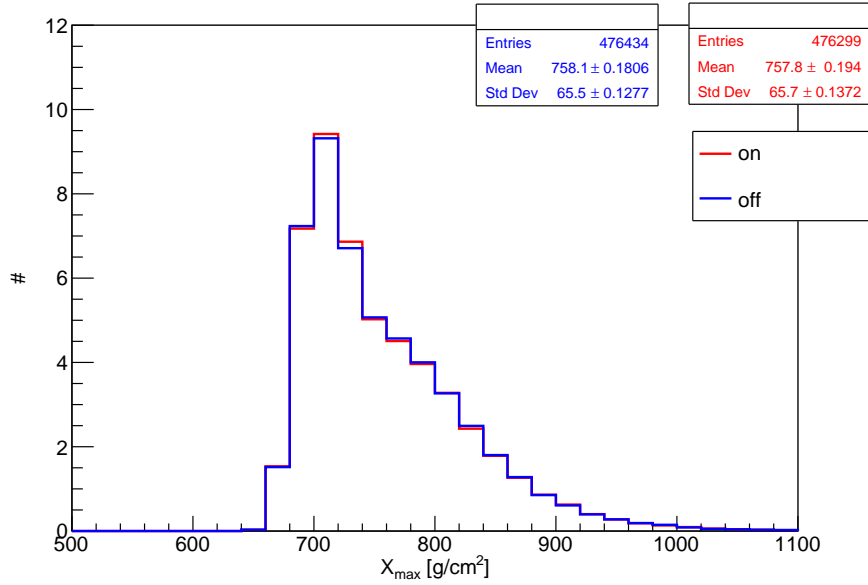
Figure 6.8: On-and off-galactic plane distributions of $X_{\max}$ for anisotropic distribution of arrival directions to the Galaxy of 50/50 mix of protons (p) and iron nuclei (Fe) for energy above $10^{18.7}$ eV.

On-Off Galactic plane		
50%-50% proton-iron	ΔX_{max} [g/cm^2]	$\Delta\sigma(X_{max})$[g/cm^2]
Isotropic	0.1 ± 0.1	0.23 ± 0.1
Auger Dipole ($10^{18.7}$ eV)	0.3 ± 0.3	-0.2 ± 0.2

Table 6.1: Table containing the On-Off galactic plane $\Delta\langle X_{\max}\rangle$ and $\Delta\sigma(X_{\max})$ values for extreme case

6.3   Chapter summary

To conclude this chapter, the performance of the analysis method proposed in (9) yields an insignificant result in the case of a maximum magnitude of (0.8 ± 0.4) g/cm^2 and (0.04 ± 0.02) g/cm^2 for $\Delta\langle X_{\mathrm{max}}\rangle$ and $\Delta\sigma(X_{\mathrm{max}})$ respectively (see Appendix .4 for $\Delta\sigma(X_{\mathrm{max}})$). These findings do not align with the observed values of (9.1 ± 1.6) g/cm^2 and (5.9 ± 2.9) g/cm^2 for $\Delta\langle X_{\mathrm{max}}\rangle$ and $\Delta\sigma(X_{\mathrm{max}})$ respectively, at energies greater than $10^{18.7}$ eV as observed in (9), indicating the absence of mass-dependent anisotropy.

Chapter 7

Mass-dependent anisotropy as a consequence of Galactic magnetic field using on-off dipole selection

In the initial analysis presented in Chapter 6, no significant values of $\Delta\langle X_{\max}\rangle$ were obtained, which required further investigation in this chapter. Here, we explore the impact of the GMF on the mass-dependent anisotropy in the arrival directions of the particles with energies above $10^{18.7}$ eV, as observed in (9). As in the previous chapter, four particle types were propagated within the GMF using the CRPropa 3 simulations. However, this time, the simulated particles are categorised according to their on-off dipole arrival direction, following the methodology outlined by (11). The dipole of interest is the Auger-like dipole described in Section 6.2. Particles arriving from 0 to 196 ° in the right ascension are classified as on-dipole, while all other particle directions are deemed off-dipole. The cut value of 196 ° was established using Figure 7.1, where the dipole fit intersects the unit line. The analysis is then carried out for the mixtures of four primary particles (p, He, N, Fe) that are constructed by their division into relative fractions by 10%, resulting in a total of 286 possible combinations.

In the following sections of this chapter, we will investigate the anisotropic distribution of simulated particles entering the Galaxy and subsequently analysing the effect of $\Delta\langle X_{\max}\rangle$ for the on-off dipole in relation to $\langle\ln(A)\rangle$ and $\sigma^2(\ln(A))$. The last section includes a specific case for the $\Delta\langle X_{\max}\rangle$ distribution of the on-off dipole a mixture of 50% - 50% proton - iron. All analyses carried out in this chapter yielded significant values in $\Delta\langle X_{\max}\rangle$ and $\Delta\sigma(X_{\max})$, (see Appendix .4 for $\Delta\sigma(X_{\max})$), however, their magnitudes do not reach the observed values of (9.1 ± 1.6) g/cm^2 and (5.9 ± 2.1) g/cm^2 for $\Delta\langle X_{\max}\rangle$ and $\Delta\sigma(X_{\max})$, respectively, as described in (9). However, the analysis presented here demonstrates mass-dependent anisotropy.
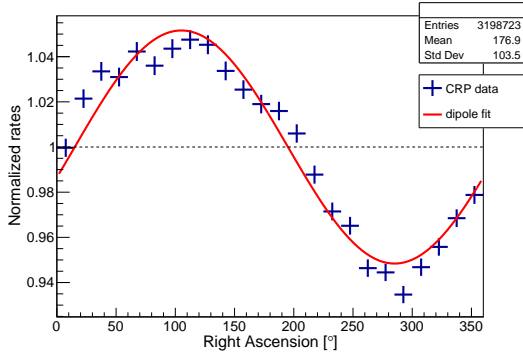
Figure 7.1: Fine tuned distribution in R.A of the normalized rates of events to match (11). Red line represents the dipole fit of the simulated data to the first harmonic.
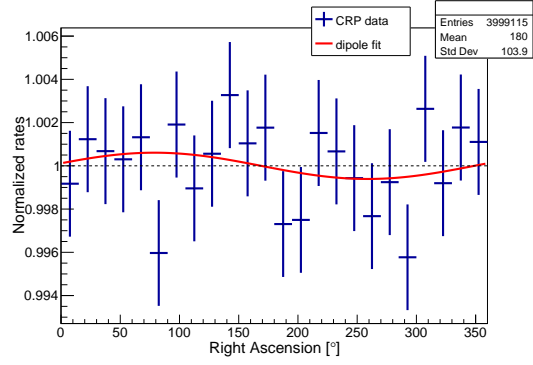
Figure 7.2: Isotropic distribution in R.A of the normalized rates of events. Red line represents the dipole fit of the simulated data to the first harmonic.

7.1   Anisotropic

7.1.1 $\Delta\langle X_{\mathrm{max}}\rangle$ relation with Energy

To study the potential energy dependence or include possible systematic uncertainties in the energy calibration, several energy thresholds were chosen for the analysis in steps of 0.5 in log E. No obvious energy dependence of $\Delta\langle X_{\mathrm{max}}\rangle$ was found; see Figure: 7.3 which represents the extreme case of the relationship between $\Delta\langle X_{\mathrm{max}}\rangle$ for on-off dipole and its corresponding energy thresholds.

Figure 7.3: $\Delta\langle X_{\mathrm{max}}\rangle$ for on-off dipole and its corresponding energy thresholds.

58

7.1.2 $\Delta\langle X_{\mathbf{max}}\rangle$ vs ln(A)
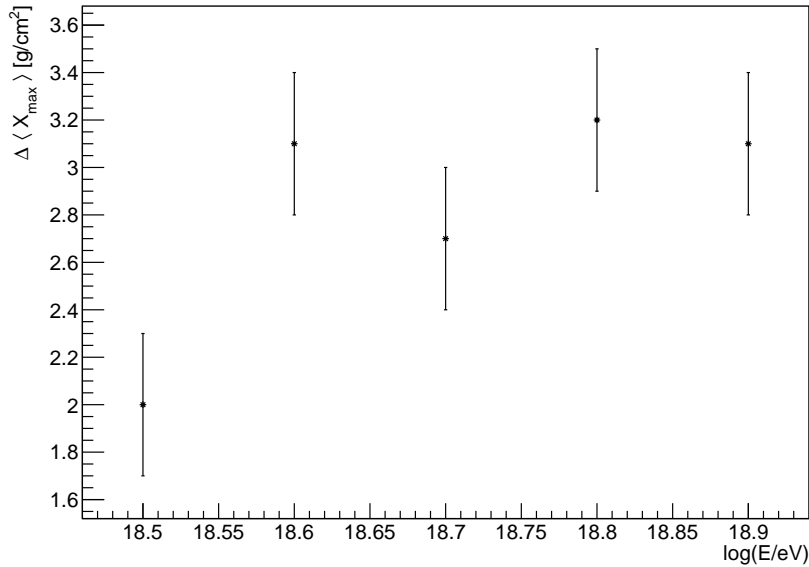
In this section, we focus on particle energies above $10^{18.7}$ eV in which we obtained significant $\Delta\langle X_{\max}\rangle$ for the on-off dipole, with a maximal value of (3.3 ± 0.5) g/cm^2 see Figure: 7.4. The overall behaviour displays a familiar "umbrella shape" histogram (2). This implies that there is a correlation between $\Delta\langle X_{\max}\rangle$ and $\langle\ln(A)\rangle$, suggesting that mass-dependent anisotropy is associated with the size of cosmic ray composition mixing.

Figure 7.4: For energy above $10^{18.7}$ eV, all 286 possible mixed compositions of p, He, N and Fe with anisotropic distribution of arrival directions to the Galaxy are represented as a plot of $\Delta\langle X_{\max}\rangle$ versus $\langle\ln(A)\rangle$.

7.1.3 $\Delta\langle X_{\mathbf{max}}\rangle$ vs $\sigma^2(\mathbf{ln(A)})$

Similarly to the previous section, the $\Delta\langle X_{\max}\rangle$ for the on-off dipole varies from
the minimum (-0.1 $\pm$ 0.2) g/cm^2 to the maximum (3.3 $\pm$ 0.5) g/cm^2 value for
energies above $10^{18.7}$ eV, see Figure: 7.5. The overall behaviour displays tightly
concentrated points along a line showing an increasing behaviour of $\Delta\langle X_{\max}\rangle$ with
respect to $\sigma^2(\ln(A))$, this implies that there is not much variation for $\Delta\langle X_{\max}\rangle$ with
increasing mix compositions, meaning that the $\Delta\langle X_{\max}\rangle$ values do not fluctuate for
each composition mix when coming from a single extragalatic dipole, and therefore
similarly to Section 7.1.2 it suggests that a mass-dependent anisotropy correlates
with the size of cosmic ray composition mixing.
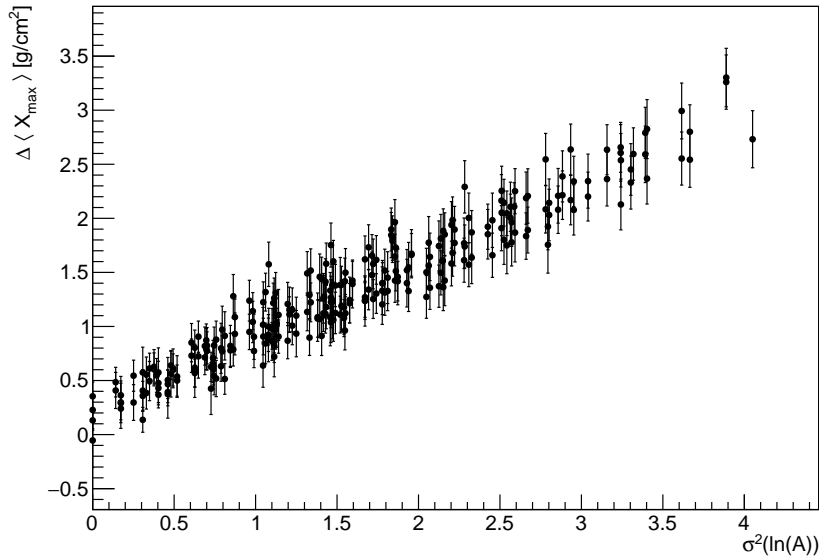
Figure 7.5: For energy above $10^{18.7}$ eV all 286 possible mixed compositions of p,
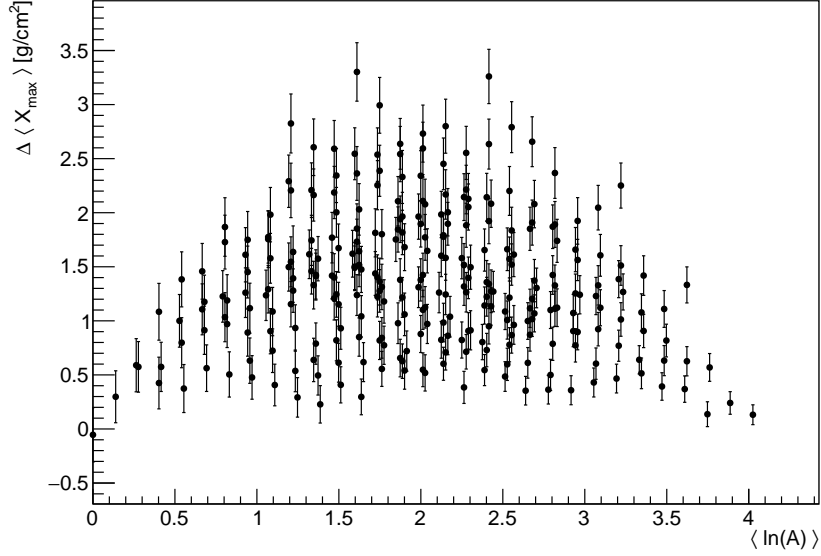He, N and Fe with anisotropic distribution of arrival directions to the Galaxy are
represented as a plot of $\Delta\langle X_{\max}\rangle$ versus $\sigma^2(\ln(A))$.

7.1.4 $\Delta\langle X_{\mathbf{max}}\rangle$ of 50% - 50% proton - iron mix

The highest $\Delta\langle X_{\max}\rangle$ and $\Delta\sigma(X_{\max})$ for the on-off dipole are anticipated in the extreme case depicted in Figure: 7.6, which consists of a mixture of a 50-50% of protons and iron nuclei. A detailed examination displayed significant $\Delta\langle X_{\max}\rangle$ and $\Delta\sigma(X_{\max})$ values, which are presented in Table: 7.1, indicating a mass-dependent anisotropy behaviour towards size of cosmic ray mix. Additionally, note that these obtained values are not consistent with the values obtained in Section 7.1.2 and Section 7.1.3, which could be attributed to statistical error. However, the extreme case values are still significant.
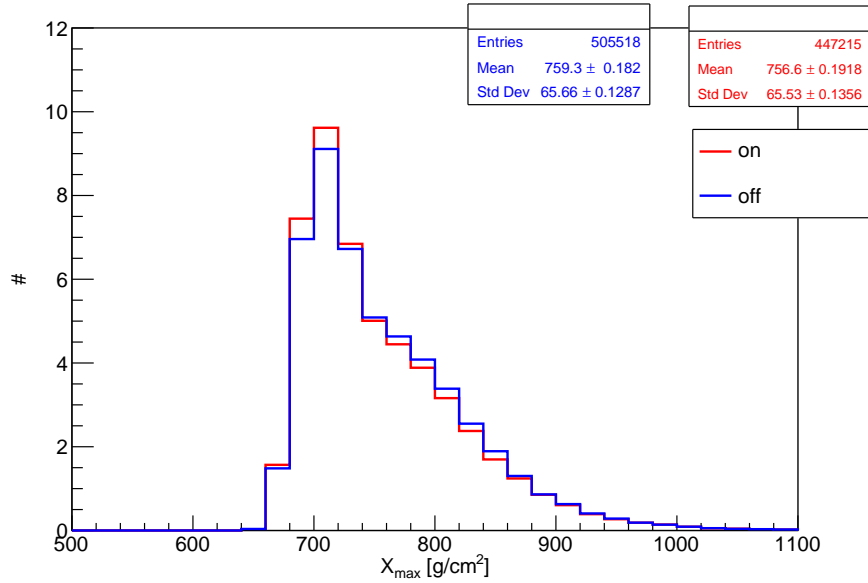
Figure 7.6: On-and off-galactic plane distributions of $X_{\max}$ for anisotropic distribution of arrival directions to the Galaxy of 50/50 mix of protons (p) and iron (Fe) nuclei for energy above $10^{18.7}$ eV.

On-Off Auger Dipole cut		
50%-50% proton-iron	ΔX_{max} [g/cm^2]	$\Delta\sigma(X_{max})$[g/cm^2]
Isotropic	0.1 ± 0.14	0.23 ± 0.1
Auger Dipole ($10^{18.7}$ eV)	2.7 ± 0.3	0.13 ± 0.3

Table 7.1: Table containing the On-Off dipole $\Delta\langle X_{\max}\rangle$ and $\Delta\sigma(X_{\max})$ values for the extreme case

7.2 Chapter summary

To conclude this chapter, the performance of the analysis method proposed in (44) yields significant results, with a maximum magnitude of (3.3 ± 0.3) g/cm^2 and (0.14 ± 0.02) g/cm^2 for $\Delta \langle X_{\max} \rangle$ and $\Delta \sigma(X_{\max})$ respectively (see Appendix .4 for $\Delta \sigma(X_{\max})$). These values did not reach the magnitudes of $\Delta \langle X_{\max} \rangle = 9.1 \pm 1.6$ [g/cm^2] and $\Delta \sigma(X_{\max}) = 5.9 \pm 2.9$ [g/cm^2] as was observed in (9). However, it did show that mass-dependent anisotropy is indeed affected by the size of cosmic ray composition mixing, when a single Auger-like dipole is considered (44).

Chapter 8

Mass-dependent anisotropy as a consequence of Galactic magnetic field influenced by properties of an extragalactic dipole

Upon the successful reproduction of a significant value for $\Delta\langle X_{\max}\rangle$ done in Chapter 7, the methodology and settings for the analysis in the following chapter will mimic Chapter 7. Hence, compositions are still split according to their on-off dipole; however, this time the extragalactic dipole has a different position and amplitude for each composition. This leads to an analysis of the effect of the GMF on the mass-dependent anisotropy in the arrival direction with respect to the change of extragalactic dipole and how they affect the mass-dependent anisotropy. This analysis is possible using a collection of 1005 individual solutions of different extragalactic dipoles provided by (12) whose obtained values fall within 2σ of the observed Auger dipole. The dipole solutions mentioned do not cover the entire ln(A) mass distribution. This is the consequence of the paper (12) that simulates particles using CRPropa3 and the JF12 GMF model and delves into the examination of the specific amplitude and dipole direction that could exhibit suppression for particular compositions, which then suggests that some solutions for specific mixes, mainly on the heavier side, did not satisfy the arrival direction within 2σ of the observed Auger dipole. For a more comprehensive analysis of the methodology used, see the above-mentioned paper.

Additional analysis of individual extragalactic dipole solutions was carried out to check if there exist directional biases in the selection of the 1005 extragalactic dipoles. Figure: 8.1 then shows that no biases are present, which was achieved by comparing the 1005 extragalactic dipole positions to its original Figure: 8.2 from (12) which consist the full number of solutions from which the selection was carried out. Additionally, the spread of the selected extragalactic dipoles is sufficient for the analysis proposed in this chapter.

In the following sections of this chapter, we will investigate the anisotropic distri-

bution of simulated particles entering the Galaxy and subsequently analysing the effect of $\Delta\langle X_{\max}\rangle$ for the on-off dipole in relation to $\langle \ln(A)\rangle$ and $\sigma^2(\ln(A))$ when in addition to the composition mixing effect, the positions of the extragalactic dipole effect are also considered. The last section includes a specific case for the $\Delta\langle X_{\max}\rangle$ distribution of the on-off dipole a mixture of 50% - 50% proton - iron. All analyses carried out in this chapter yielded significant values in $\Delta\langle X_{\max}\rangle$ and $\Delta\sigma(X_{\max})$, (see Appendix .4 for $\Delta\sigma(X_{\max})$), its magnitudes did not exceed the maximal values from the study in Chapter 7, however, the spread of $\sigma^2(ln(A))$ is much more dispersed in comparison to section 7.1.3 suggesting that the position of an extragalactic dipole has an effect on the $\Delta\langle X_{\max}\rangle$ values see Figure: 8.6 and therefore also on the mass-dependent anisotropy.
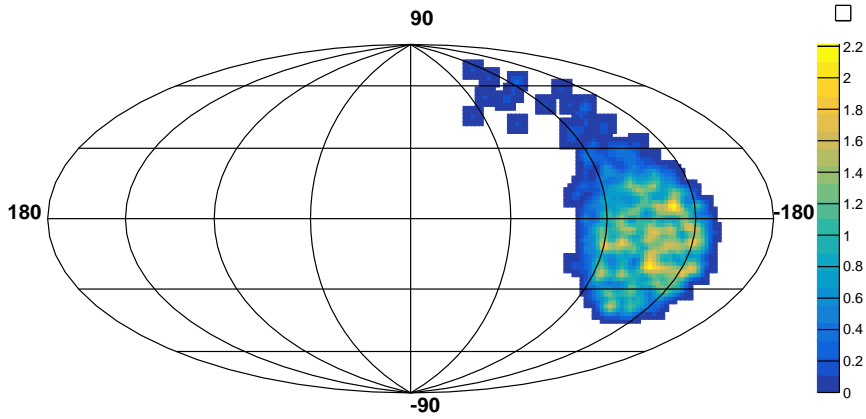
Figure 8.1: The directions of the 1005 possible solutions of extragalactic dipole whose value are within 2σ of the observed Auger dipole in Galactic coordinates with Gaussian smoothing. Z-axis represent concentration of chosen dipoles position.
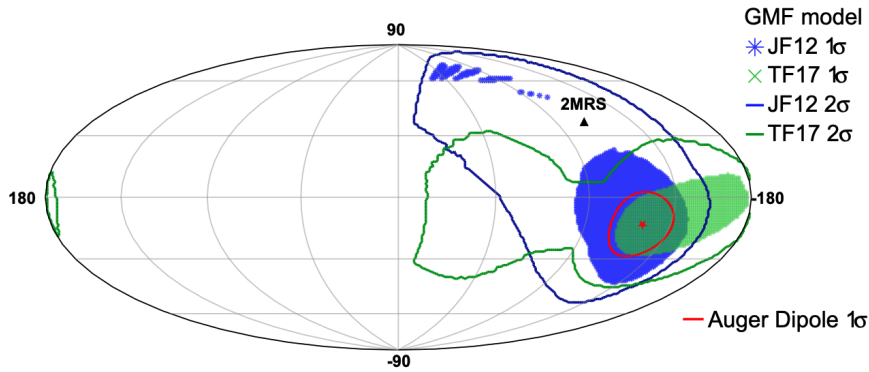
Figure 8.2: "The directions of the extragalactic dipole in Galactic coordinates found for all different mass composition scenarios for the JF12 and TF17 models of GMF within 1σ. Areas of possible directions of the extragalactic dipole compatible with the measurements within 2σ are shown by blue and green lines for JF12 and TF17 models, respectively. The 1σ contour of the dipole measured by the Pierre Auger Observatory above 8 EeV is shown in red and direction of the 2MRS dipole is displayed with a black triangle marker." Taken from (12).

8.1 Anisotropic

8.1.1 $\Delta\langle X_{\mathbf{max}}\rangle$ vs ln(A)

In this section, we focus on particle energies above $10^{18.7}$ eV in which we obtained significant $\Delta\langle X_{\max}\rangle$ for the on-off dipole, with a maximal value of (3.3 ± 0.3) g/cm^2 see Figure: 8.3. The overall behaviour displays a familiar "umbrella shape" histogram (2) with its high mass compositions missing and also the position of the highest $\Delta\langle X_{\max}\rangle$ being shifted when compared to Section 7.1.2. This implies that there might exist extragalactic dipoles position which can cause such a correlation between $\Delta\langle X_{\max}\rangle$ and $\langle\ln(A)\rangle$, in addition to the size of cosmic ray composition mixing.

Figure 8.3: For energy above $10^{18.7}$ eV, all 286 possible mixed compositions of p, He, N and Fe with anisotropic distribution of arrival directions to the Galaxy are represented as a plot of $\Delta\langle X_{\max}\rangle$ versus $\langle\ln(A)\rangle$.

8.1.2 $\Delta\langle X_{\mathbf{max}}\rangle$ vs $\sigma^2(\mathbf{ln(A)})$

Similarly to the previous section, the $\Delta\langle X_{\max}\rangle$ of on-off dipole values range from the lowest of (-0.2 ± 0.2) g/cm^2 up to the largest (3.3 ± 0.3) g/cm^2 with the the overall behaviour suggesting that there is a correlation between the size of cosmic ray composition mixing and $\Delta\langle X_{\max}\rangle$ value as shown in previous section. Additionally, Figure: 8.4 further solidifies what was obtained in previous section. It shows that different extragalactic dipoles could introduce almost a double the dispersion in the $\Delta\langle X_{\max}\rangle$ when compared to section 7.1.3, implying that there might exist extragalactic dipoles which affect the $\Delta\langle X_{\max}\rangle$ more then other.
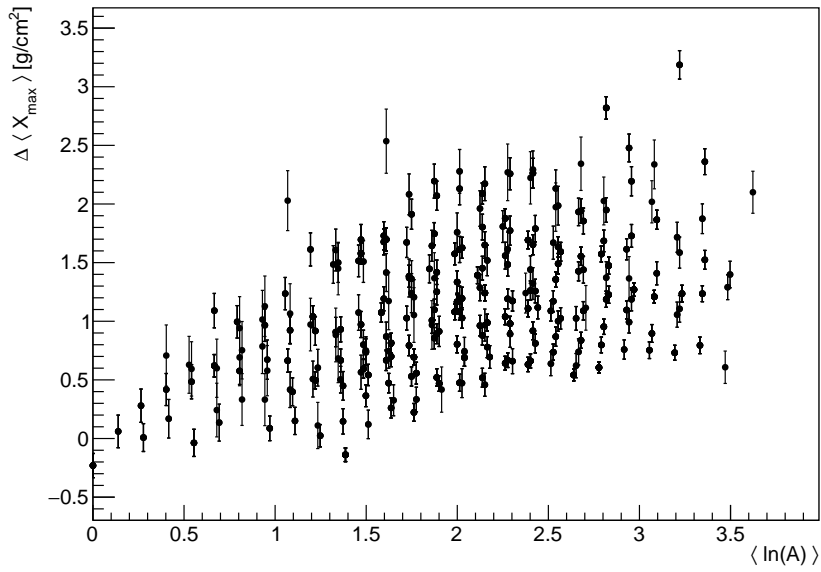

Figure 8.4: For energy above $10^{18.7}$ eV all 286 possible mixed compositions of p, He, N and Fe with anisotropic distribution of arrival directions to the Galaxy are represented as a plot of $\Delta\langle X_{\max}\rangle$ versus $\sigma^2(\ln(A))$.

8.1.3 $\Delta\langle X_{\mathbf{max}} \rangle$ of 50% - 50% proton - iron mix

The highest $\Delta\langle X_{\max} \rangle$ and $\Delta\sigma(X_{\max})$ for the on-off dipole are anticipated in the extreme case depicted in Figure: 8.5, which consists of a mixture of a 50-50% of protons and iron nuclei. A detailed examination displayed significant $\Delta\langle X_{\max} \rangle$ and $\Delta\sigma(X_{\max})$ values whose magnitudes does not surpass single case dipole in Section 7.1.4. Obtained values are presented in the Table: 8.1, indicating a mass-dependent anisotropy behaviour toward size of cosmic ray mix. In addition, note that these obtained values are not consistent with the obtained values from Section 8.1.1 and Section 8.1.2, which is due to the extragalactic dipole positions having effect on the $\Delta\langle X_{\max} \rangle$.
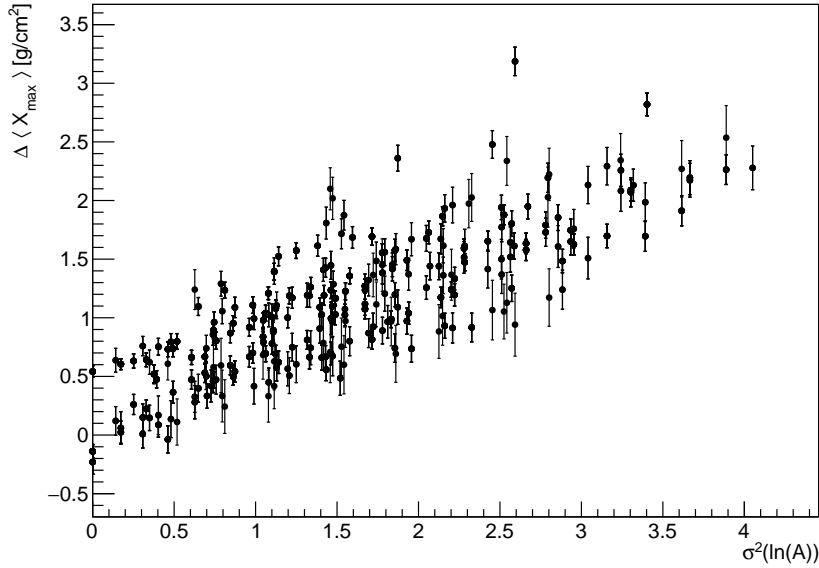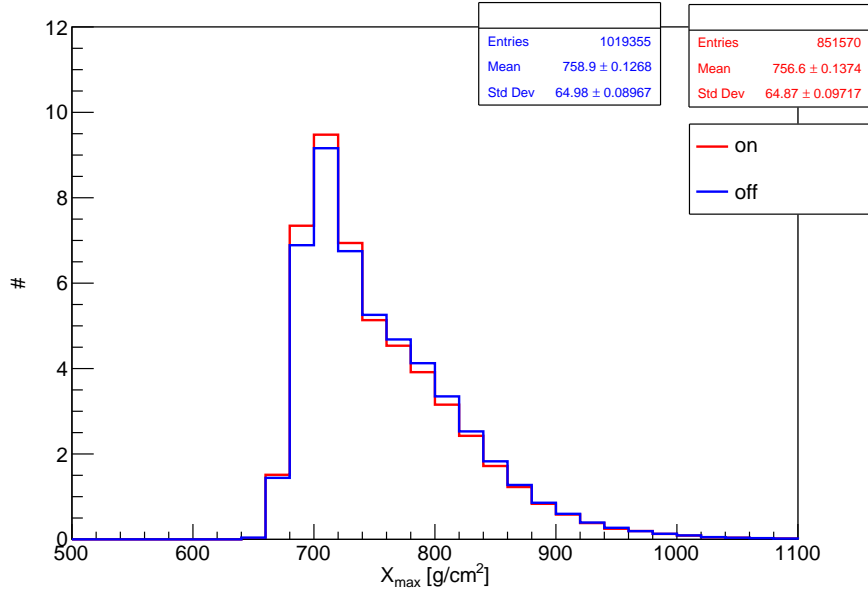

Figure 8.5: For energy above $10^{18.7}$ eV all 286 possible mixed compositions of p, He, N and Fe with anisotropic distribution of arrival directions to the Galaxy are represented as a plot of $\Delta\langle X_{\max} \rangle$ versus $\sigma^2(\ln(A))$.

On-Off Dipole cut		
50%-50% proton-iron	ΔX_{max} [g/cm^2]	$\Delta\sigma(X_{max})$[g/cm^2]
Isotropic	0.1 ± 0.14	0.23 ± 0.1
Extragalactic dipole ($10^{18.7}$ eV)	2.3 ± 0.2	0.11 ± 0.1

Table 8.1: Table containing the On-Off galactic dipole $\Delta\langle X_{\max} \rangle$ and $\Delta\sigma(X_{\max})$ for the extreme case

8.2   Chapter summary

To conclude this chapter, the performance of the analysis method proposed in Chapter 7 is also confirmed for a range of different extragalactic dipole scenarios from (12). For these scenarios, we obtained $\Delta\langle X_{\max}\rangle$ values that did not exceed the maximal values from Chapter 7 for the particular choice of an Auger-like dipole. However, Section 8.1.2 shows that the values of $\sigma^2(ln(A))$ are more dispersed when compared to a single Auger-like dipole case shown in Section 7.1.3. It suggests that the position of an extragalactic dipole has an effect on the $\Delta\langle X_{\max}\rangle$ values, and therefore the mass-dependent anisotropic behaviour is a consequence of both the mass composition of cosmic rays and also the position and amplitude of the extragalactic dipole. The strongest effect was observed for extragalactic dipoles of lon $>$ -90° and also values above lat $>$ 30° as per Figure: 8.6
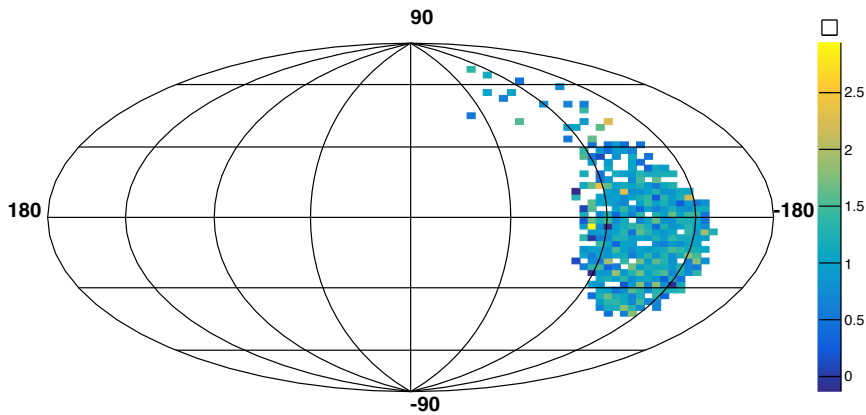

Figure 8.6: The directions of the 1005 possible solutions of extragalactic dipole whose value are within 2σ of the observed Auger dipole in Galactic coordinates. Here the Z-axis results represent the on-off dipole $\Delta\langle X_{\max}\rangle$ values for each chosen dipoles position.

Conclusions

This diploma thesis was dedicated to reproduce the aspects of the mass-dependent anisotropy in arrival directions of cosmic rays with respect to the Galactic plane that was observed by the Piere Auger Observatory above energy of $10^{18.7}$ eV (9). We studied two factors influencing such observation: mass composition of cosmic rays and the properties of the extragalactic dipole, assuming one particular model of the Galactic magnetic field (GMF). To closely analyse the above-mentioned effects, simulations using an open-source framework called CRPropa 3 in three-dimensional mode were used. For these simulations, the particles were backtracked as antiparticles from Earth through the JF12 GMF (Section 2.2) to the edge of the Galaxy; see Section 5.1.

In the first analysis that was performed in Chapter 6, the methodology of on-off galactic-plane selection of simulated particles according to their arrival directions was applied as in (9). It resulted in non significant values of the change of average mass-dependent parameter $\Delta\langle X_{\max}\rangle < \pm 0.3$ g/cm^2 and its fluctuations $\Delta\sigma(X_{\max})$ = (-0.2 $\pm$ 0.2) g/cm^2, for the most extreme case of the 50/50 mix of protons and iron nuclei, even for various ranges of energy. This is in contradiction with what was observed in (9).

As the main result of the thesis, a modified analysis was proposed and performed in Chapter 7. This time the methodology of on-off dipole selection was applied, based on the observation in (44). The particles were divided according to their arrival directions with respect to excess and lack of the observed dipole in the right ascension. In such a particle division, values of $\Delta\langle X_{\max}\rangle$ = (2.7 $\pm$ 0.3) g/cm^2 and $\Delta\sigma(X_{\max})$ = (0.13 $\pm$ 0.3) g/cm^2 were found for the most extreme case of the 50/50 mix of protons and iron nuclei. We did not obtain the magnitudes observed in (9) even for such an event division; however, we showed that the mass-dependent anisotropy correlates with the size of the mixing of mass composition of cosmic rays when properties of one specific extragalactic dipole were assumed.

The final analysis done in Chapter 8 tests how much the mass-dependent anisotropy depends on the properties of an extragalactic dipole. The wide space of solutions for primary fractions and dipole properties obtained from the author of (12) was used for such a purpose, taking into account the effect of GMF using the JF12 model. The results using on-off dipole selection suggest that the properties of the extragalatic dipole affect the values of $\Delta\langle X_{\max}\rangle$, leading to the conclusion that the mass-dependent anisotropy of the arrival directions of particles is sensitive to the size of mixing of mass composition and also to the specific extragalatic dipole position,

with the strongest effect for dipole directions of galactic longitudes $> -90°$ and also above galatic latitudes $> 30°$. Therefore, the maximal mass-dependent anisotropy signal can be obtained even for a not maximally mixed beam of primary particles for specific properties of the extragalactic dipole.

Bibliography

[1] S. Mollerach, E. Roulet, Progress in high-energy cosmic ray physics, Progress in Particle and Nuclear Physics 98 (2018) 85–118. `doi:https://doi.org/10.1016/j.ppnp.2017.10.002`.

[2] K.-H. Kampert, et al., Measurements of the cosmic ray composition with air shower experiments, Astroparticle Physics 35 (10) (2012) 660–678. `doi:10.1016/j.astropartphys.2012.02.004`.

[3] R. Jansson, G. R. Farrar, A new model of the galactic magnetic field, The Astrophysical Journal 757 (1) (2012) 14. `doi:10.1088/0004-637x/757/1/14`. URL `http://dx.doi.org/10.1088/0004-637X/757/1/14`

[4] The pierre auger cosmic ray observatory, Nuclear Instruments and Methods in Physics Research Section A: Accelerators, Spectrometers, Detectors and Associated Equipment 798 (2015) 172–213. `doi:https://doi.org/10.1016/j.nima.2015.06.058`.

[5] A. Aab, P. Abreu, et al., Measurement of the cosmic-ray energy spectrum above 2.5× 10 18 ev using the pierre auger observatory, Physical Review D 102 (6) (2020) 062005. `doi:https://doi.org/10.1103/PhysRevD.102.062005`.

[6] P. Abreu, et al., The energy spectrum of cosmic rays beyond the turn-down around 10^ 17 10 17 ev as measured with the surface detector of the pierre auger observatory, The European Physical Journal C 81 (2021) 1–25. `doi:https://doi.org/10.1140/epjc/s10052-021-09700-w`.

[7] A. Aab, P. A. et al., Evidence for a mixed mass composition at the 'ankle' in the cosmic-ray spectrum, Physics Letters B 762 (2016) 288–295. `doi:https://doi.org/10.1016/j.physletb.2016.09.039`.

[8] A. Coleman, et al., Ultra high energy cosmic rays the intersection of the cosmic and energy frontiers, Astroparticle Physics 147 (2023) 102794. `doi:https://doi.org/10.1016/j.astropartphys.2022.102794`.

[9] E. Mayotte, et al., Indication of a mass-dependent anisotropy above 10 18.7 ev in the hybrid data of the pierre auger observatory (2022). `doi:10.22323/1.395.0321`.

[10] R. A. Batista, et al., Crpropa 3—a public astrophysical simulation framework for propagating extraterrestrial ultra-high energy particles, Journal of Cosmology and Astroparticle Physics 2016 (05) (2016) 038–038. `doi:10.1088/1475-7516/2016/05/038`.

[11] P. A. Collaboration, A. Aab, P. Abreu, et al., Observation of a large-scale anisotropy in the arrival directions of cosmic rays above 8×1018 ev, Science 357 (6357) (2017) 1266–1270. `doi:10.1126/science.aan4338`.

[12] A. Bakalová, J. Vícha, P. Trávníček, Modification of the Dipole in Arrival Directions of Ultra-high-energy Cosmic Rays due to the Galactic Magnetic Field (3 2023). `arXiv:2303.08766`.

[13] V. F. Hess, Über den ursprung der durchdringenden strahlung, Z. Phys. 14 (1913) 610.

[14] L. Cazon, The pierre auger observatory: new results and prospects, arXiv preprint arXiv:1808.00745 (2018).
URL `https://arxiv.org/abs/1808.00745`

[15] J. Linsley, Primary cosmic rays of energy 1017 to 1020 ev, the energy spectrum and arrival directions, in: International Cosmic Ray Conference, Vol. 4, 1963, p. 77.

[16] J. Bellido, Depth of maximum of air-shower profiles at the Pierre Auger Observatory: Measurements above $10^{17.2}$ eV and Composition Implications, PoS ICRC2017 (2017) 506. `doi:10.22323/1.301.0506`.

[17] N. Globus, et al., Propagation of high-energy cosmic rays in extragalactic turbulent magnetic fields: resulting energy spectrum and composition, Astronomy & Astrophysics 479 (1) (2008) 97–110. `doi:https://doi.org/10.1051/0004-6361:20078653`.

[18] I. V. Dorman, Cosmic rays, Moscow Izdatel Nauka (Jan. 1981).

[19] A. Haungs, et al., Investigating the 2nd knee: The kascade-grande experiment, in: Journal of Physics: Conference Series, Vol. 47, IOP Publishing, 2006, p. 029. `doi:10.1088/1742-6596/47/1/029`.

[20] M. Unger, G. R. Farrar, L. A. Anchordoqui, Origin of the ankle in the ultrahigh energy cosmic ray spectrum, and of the extragalactic protons below it, Physical Review D 92 (12) (2015) 123001. `doi:https://doi.org/10.1103/PhysRevD.92.123001`.

[21] B. Peters, Primary cosmic radiation and extensive air showers, Il Nuovo Cimento (1955-1965) 22 (4) (1961) 800–819. `doi:https://doi.org/10.1007/BF02783106`.

[22] K. Greisen, End to the cosmic-ray spectrum?, Physical Review Letters 16 (17) (1966) 748. `doi:https://doi.org/10.1103/PhysRevLett.16.748`.

[23] G. T. Zatsepin, V. A. Kuz'min, Upper limit of the spectrum of cosmic rays, Soviet Journal of Experimental and Theoretical Physics Letters 4 (1966) 78.
URL http://www.jetpletters.ru/ps/1624/article_24846.shtml

[24] K. Greisen, Cosmic ray showers, Annual Review of Nuclear Science 10 (1) (1960) 63–108. doi:10.1146/annurev.ns.10.120160.000431.

[25] A. Aab, P. Abreu, et al., Depth of maximum of air-shower profiles at the pierre auger observatory. i. measurements at energies above $10^{17.8}$ eV, Phys. Rev. D 90 (2014) 122005. doi:10.1103/PhysRevD.90.122005.

[26] J. C. Mather, E. Cheng, et al., Measurement of the cosmic microwave background spectrum by the cobe firas instrument, The Astrophysical Journal 420 (1994) 439–444. doi:10.1086/173574.

[27] A. Bakalová, Connection between energy spectrum, mass composition and distribution of sources of extragalactic cosmic rays, Experimental Nuclear and Particle Physics 4.
URL http://hdl.handle.net/10467/76304

[28] D. Kuempel, Extragalactic propagation of ultra-high energy cosmic rays (2014). arXiv:1409.3129.

[29] L. M. Widrow, Origin of galactic and extragalactic magnetic fields, Rev. Mod. Phys. 74 (2002) 775–823. doi:10.1103/RevModPhys.74.775.

[30] R. M. Crutcher, Magnetic fields in molecular clouds, Annual Review of Astronomy and Astrophysics 50 (2012) 29–63. doi:https://doi.org/10.1146/annurev-astro-081811-125514.

[31] M. S. Pshirkov, P. G. Tinyakov, et al., Deriving the global structure of the galactic magnetic field from faraday rotation measures of extragalactic sources, The Astrophysical Journal 738 (2) (2011) 192. doi:10.1088/0004-637x/738/2/192.

[32] E. Lopez-Rodriguez, Guerra, et al., The strength and structure of the magnetic field in the galactic outflow of messier 82, The Astrophysical Journal 914 (1) (2021) 24. doi:10.3847/1538-4357/abf934.

[33] M. Ackermann, M. Ajello, et al., Detection of the characteristic pion-decay signature in supernova remnants, Science 339 (6121) (2013) 807–811. doi:10.1126/science.1231160.

[34] J. Brown, et al., Rotation measures of extragalactic sources behind the southern galactic plane: New insights into the large-scale magnetic field of the inner milky way, The Astrophysical Journal 663 (1) (2007) 258. doi:10.1086/518499.

[35] V. Heesen, R. Beck, M. Krause, R.-J. Dettmar, Cosmic rays and the magnetic field in the nearby starburst galaxy ngc 253-i. the distribution and transport of cosmic rays, Astronomy & Astrophysics 494 (2) (2009) 563–577. doi:https://doi.org/10.1051/0004-6361:200810543.

[36] K. Dolag, D. Grasso, V. Springel, I. Tkachev, Mapping deflections of extragalactic ultra high energy cosmic rays in magnetohydrodynamic simulations of the local universe, Nuclear Physics B-Proceedings Supplements 136 (2004) 234–243. doi:https://doi.org/10.1016/j.nuclphysbps.2004.10.030.

[37] K. Enqvist, Primordial magnetic fields, International Journal of Modern Physics D 7 (03) (1998) 331–349. doi:https://doi.org/10.1142/S0218271898000243.

[38] J. P. Conlon, F. V. Day, 3.55 kev photon lines from axion to photon conversion in the milky way and m31, Journal of Cosmology and Astroparticle Physics 2014 (11) (2014) 033. doi:10.1088/1475-7516/2014/11/033.

[39] T. P. A. Collaboration, Timeline of the pierre auger observatory, accessed: 2023-04-30 (2023).
URL https://www.auger.org/observatory/timeline-observatory

[40] J. Abraham, et al., The fluorescence detector of the pierre auger observatory 620 (2-3) (2010) 227–251. doi:https://doi.org/10.1016/j.nima.2010.04.023.

[41] C. Bonifazi, The angular resolution of the pierre auger observatory, Nuclear Physics B - Proceedings Supplements 190 (2009) 20–25, proceedings of the Cosmic Ray International Seminars. doi:https://doi.org/10.1016/j.nuclphysbps.2009.03.063.

[42] B. R. Dawson, H. Y. Dai, P. Sommers, S. Yoshida, Simulations of a giant hybrid air shower detector, Astroparticle Physics 5 (1996) 239–247. doi:10.1016/0927-6505(96)00024-2.

[43] R. A. Gideon, R. A. Hollister, A rank correlation coefficient resistant to outliers, Journal of the American Statistical Association 82 (398) (1987) 656–666. doi:10.1080/01621459.1987.10478480.

[44] A. Aab, P. Abreu, M. Aglietta, et al., Large-scale cosmic-ray anisotropies above 4 eev measured by the pierre auger observatory, The Astrophysical Journal 868 (1) (2018) 4. doi:10.3847/1538-4357/aae689.

[45] T. P. A. Collaboration, Realsimhybrid, https://www.auger.unam.mx/AugerWiki/RealSimHybrid, accessed: 2023-04-29 (2023).
URL https://www.auger.unam.mx/AugerWiki/RealSimHybrid

[46] S. Argiro, S. Barroso, J. Gonzalez, et al., The offline software framework of the pierre auger observatory, Nuclear Instruments and Methods in Physics Research Section A: Accelerators, Spectrometers, Detectors and Associated Equipment 580 (3) (2007) 1485–1496. doi:https://doi.org/10.1016/j.nima.2007.07.010.

[47] T. Pierog, M. Alekseeva, T. Bergmann, et al., First results of fast one-dimensional hybrid simulation of eas using conex, Nuclear Physics B - Proceedings Supplements 151 (1) (2006) 159–162. doi:https://doi.org/10.1016/j.nuclphysbps.2005.07.029.

[48] T. R. Team, Root: A data analysis framework, accessed: 2023-04-29 (2023).
URL `https://root.cern.ch/`

[49] K. Cooray, Generalized gumbel distribution, Journal of Applied Statistics 37 (1)
(2010) 171–179. `doi:10.1080/02664760802698995`.

[50] M. De Domenico, M. Settimo, et al., Reinterpreting the development of extensive air showers initiated by nuclei and photons, Journal of Cosmology and Astroparticle Physics 2013 (7) (2013). `arXiv:1305.2331`, `doi:10.1088/1475-7516/2013/07/050`.

.1 CRPropa 3 python code

```python
from crpropa import *

#Magnetic field
randomSeed = 42
B = JF12Field()
B.randomStriated(randomSeed)
B.randomTurbulent(randomSeed)

#primar
A =[1,2,7,26]
Z =[1,4,14,56]
name = ["p","He","N","Fe"]

#Loop for each primar
for i in range(len(A)):
    #Simulation Setup
    simulation = ModuleList()
    simulation.add(PropagationCK(B, 1e-5, 1 * pc, 1 * kpc))
    simulation.add(MaximumTrajectoryLength(1 * Mpc))

    #Create  module that sets the observer location
    observer = Observer()
    observer.add(ObserverLargeSphere(Vector3d(0), 20 * kpc))
    simulation.add(observer)

    #Generate particles from the source
    source = Source()
    source.add(SourcePosition(Vector3d(-8.5,0,0) * kpc))
    source.add(SourceIsotropicEmission()  )

    #add partidle generator for source
    source.add(SourceParticleType(- nucleusId(Z[i], A[i])))
    source.add(SourcePowerLawSpectrum(3.16 * EeV,
                                      100 * EeV,  -1))

    #Output and specific info to be writen to .txt
    output1 = TextOutput('JF12Backtracking_'+name[i],
                         +'_18.5-20.0.txt',
                         Output.Trajectory3D)

    output1.setLengthScale(kpc)
    output1.disableAll()
    output1.enable(Output.TrajectoryLengthColumn)
    output1.enable(Output.CurrentIdColumn)
    output1.enable(Output.CurrentEnergyColumn)
```

```
output1.enable(Output.CurrentPositionColumn)
output1.enable(Output.CurrentDirectionColumn)
output1.enable(Output.CreatedPositionColumn)
output1.enable(Output.CreatedDirectionColumn)
output1.enable(Output.SerialNumberColumn)

observer.onDetection(output1)

simulation.setShowProgress(True) #(tqdm)
simulation.run(source, 1000000) #n for gen.
```

.2 CRPropa 3 back-tracking simulation validation

As mentioned previously, the approach selected for CRPropa in this study is the backtracking method. To verify the precision of the results produced, a comparison is conducted at an energy level of 8 EeV with the forward tracking method. The simulated particles used for this analysis are smaller in size consisting of 100,000 generated particles per element and are provided by (12).

Figure: 7 and Figure: 8 exhibit identical behaviour, confirming the consistency between the two methods. Furthermore, Figure: 9 and Figure: 10 for the on-off-dipole scenarios demonstrate reasonable similarities, indicating that the chosen energy level yields comparable results for both propagation methods. This observation also applies to Figure: 11 and Figure: 12, which represent on- and off-galactic plane situations.

In conclusion, the performance of CRPropa 3 is consistent between the backtracking and forward tracking methods. Allowing to use the backtracing method in the final product for this diploma thesis.
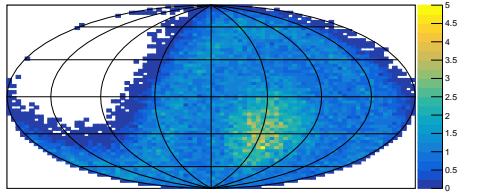

Figure 7: Forward tracking Mollweide projection of arrival directions in galactic coordinates, with Auger-Dipole. Z-axis represents the flux intensity. Energy cut 8 EeV up to 100 EeV.
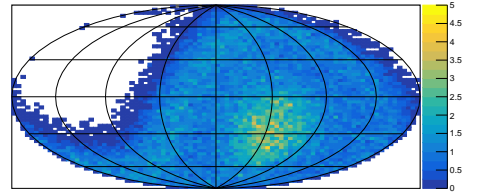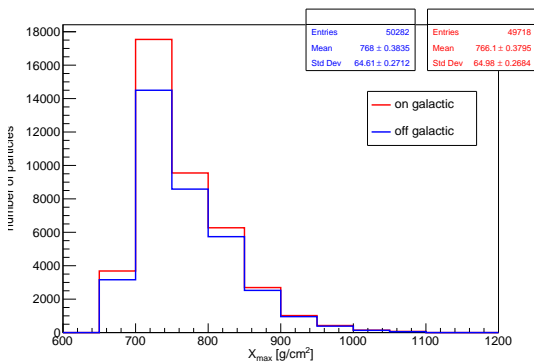

Figure 8: Back tracking Mollweide projection of arrival directions in galactic coordinates, with Auger-Dipole. Z-axis represents the flux intensity. Energy cut 8 EeV up to 100 EeV.

Figure 9: Forward tracking of the on-off dipole cut X_{max} value for specific mix composition of 50-50 proton/iron.
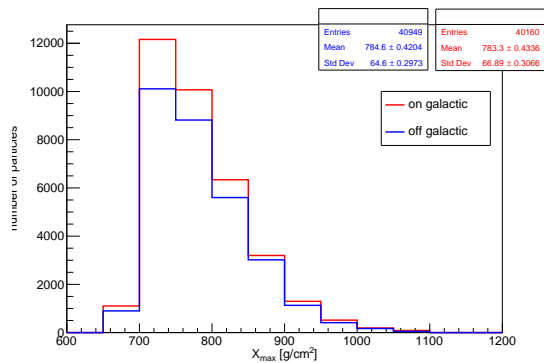

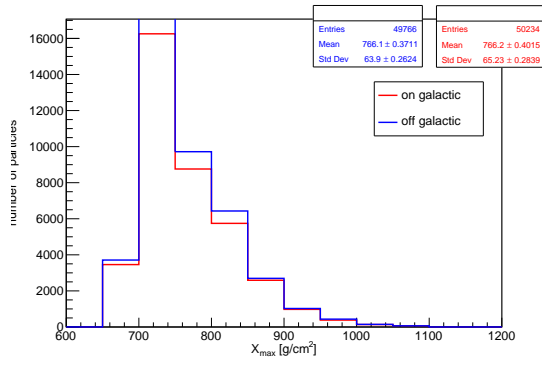Figure 10: Back tracking of the on-off dipole cut X_{max} value for specific mix composition of 50-50 proton/iron.

Figure 11: Forward tracking of the on-off galactic cut X_{max} value for specific mix composition of 50-50 proton/iron.
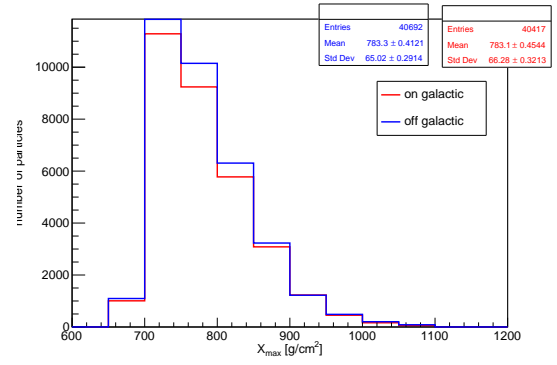
Figure 12: Back tracking of the on-off galactic cut X_{max} value for specific mix composition of 50-50 proton/iron.

.3 Additional $\Delta\langle X_{\mathbf{max}}\rangle$ and $\sigma^2(\ln(A))$ analysis

In this section, an additional analysis on the $\Delta\langle X_{\max}\rangle$ and $\sigma^2(\ln(A))$ for 1005 extragalatic dipole solutions used in Chapter 8 but instead uses the galactic on-off plane split, which results in no significant values.
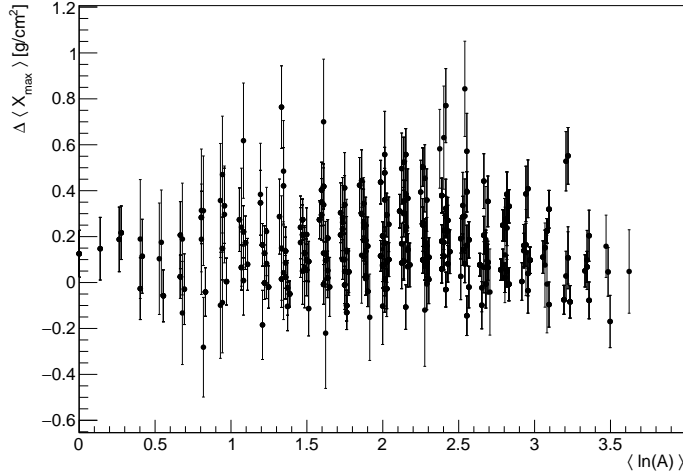

Figure 13: For energy above $10^{18.7}$ eV, all 267 possible mixed compositions of p, He, N and Fe with anisotropic distribution of arrival directions to the Galaxy are represented as a plot of $\Delta\langle X_{\max}\rangle$ versus $\langle\ln(A)\rangle$ using the on-off galactic plane split.
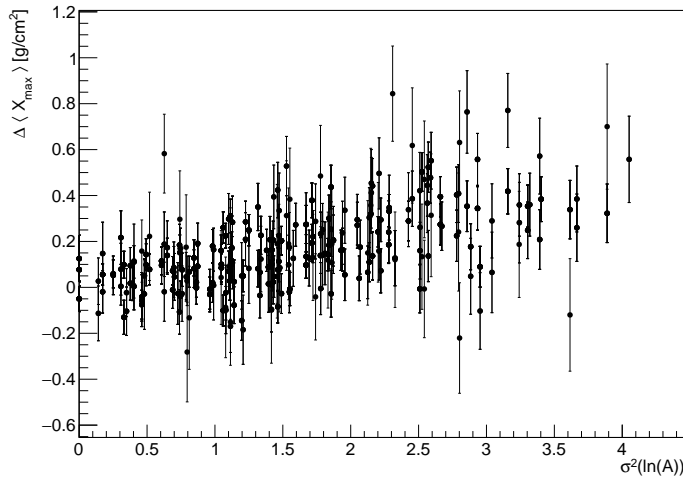

Figure 14: For energy above $10^{18.7}$ eV all 286 possible mixed compositions of p, He, N and Fe with anisotropic distribution of arrival directions to the Galaxy are represented as a plot of $\Delta\langle X_{\max}\rangle$ versus $\sigma^2(\ln(A))$ using the on-off galactic plane split.

.4 Additional $\sigma(\mathrm{X}_{max})$ analysis

In this section, an additional analysis on the $\sigma(\mathrm{X}_{max})$ for the Auger-like dipole utilised in Chapter 6 and Chapter 7 and the 1005 solutions of extragalatic dipoles utilised in Chapter 7 is done.

$\sigma(\mathrm{X}_{max})$ values for Auger-like dipole for both on-off galactic and on-off dipole is shown in Figure: 15 and Figure: 16 respectively.
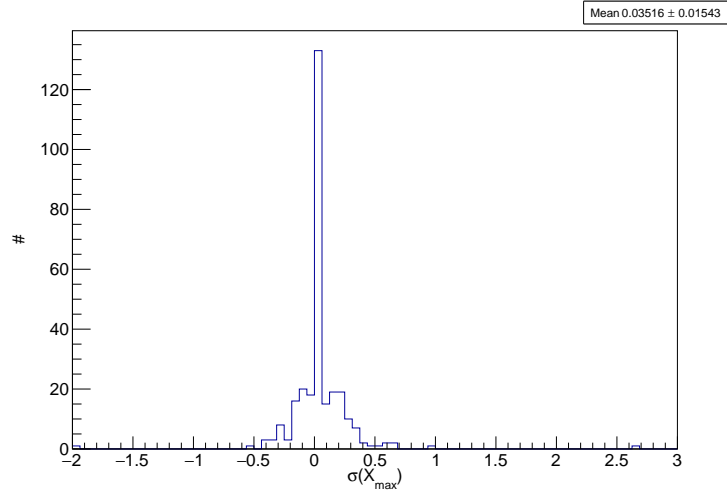

Figure 15: The histogram represents all possible $\sigma(\mathrm{X}_{max})$ of Auger-like dipole for energies above $10^{18.7}$ eV, using an on-off galactic split.
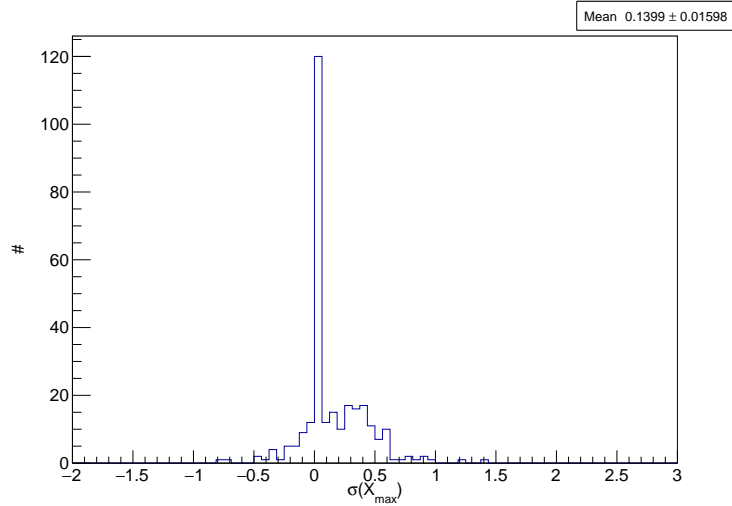

Figure 16: The histogram represents all possible $\sigma(\mathrm{X}_{max})$ of the Auger-like dipole for energies above $10^{18.7}$ eV, using on-off dipole split.

$\sigma(\mathrm{X}_{max})$ values for chosen 1005 extragalatic dipoles for on-off dipole are shown in Figure: 17.
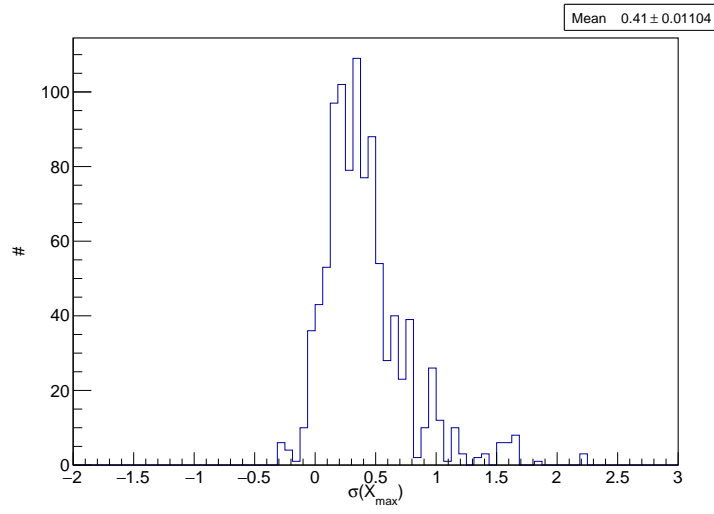

Figure 17: The histogram represents all possible $\sigma(\mathrm{X}_{max})$of range of extragalactic dipoles for energies above $10^{18.7}$ eV, using on-off dipole split.